Inhibition of HIV infection by structural proteins of the inner nuclear membrane is associated with reduced chromatin dynamics

Anvita Bhargava[1], Mathieu Maurin[1], Patricia M. Davidson[2,@], Mabel Jouve[3], Xavier Lahaye[1,#], Nicolas Manel[1,#]

[1] Institut Curie, PSL Research University, INSERM U932, Paris, France.

[2] Laboratoire Physico-Chimie Curie, Institut Curie, CNRS UMR168, Sorbonne Université, PSL Research University, Paris, France.

[3] Institute Curie, UMR3215, Paris, France.

Correspondance : nicolas.manel@curie.fr

# Equal contribution

@ current address: Now at 4Dcell, Montreuil, France.

Abstract

The Human Immunodeficiency Virus (HIV) enters the nucleus to establish infection. HIV interacts with nuclear pore components to cross the nuclear envelope. In contrast, the role of other proteins of the nuclear envelope in HIV infection is not yet understood. The inner nuclear transmembrane proteins SUN1 and SUN2 connect lamins in the interior of the nucleus to the cytoskeleton in the cytoplasm. Increased levels of SUN1 or SUN2 potently restrict HIV infection through an unresolved mechanism. Here, we find that SUN1 and SUN2 exhibit a differential and viral strain-specific antiviral activity HIV-1 and HIV-2. In macrophages and HeLa cells, HIV-1 and HIV-2 are respectively preferentially inhibited by SUN1 and SUN2. This specificity maps to the nucleoplasmic domain of SUN proteins, which associates with Lamin A/C and participates to the DNA damage response. We find that etoposide, a DNA-damaging drug, stimulates infection. Inhibition of the DNA damage signaling kinase ATR, which induces a DNA damage response, also enhances HIV-1 infection. The proviral effect of ATR inhibition on infection requires the HIV-1 Vpr gene. Depletion of endogenous Lamin A/C, which sensitizes cells to DNA damage, also enhances HIV-1 infection in HeLa cells. SUN1 overexpression neutralizes these proviral effects, while the antiviral effect of SUN2 is rescued by etoposide treatment. Finally, we show that inhibition of HIV-1 infection by overexpressed SUN proteins and endogenous Lamin A/C is associated with reduced internal movements of chromatin and reduced rotations of the nucleus. Altogether, these results highlight distinct antiviral activities of SUN1 and SUN2 and reveal an emerging role of nuclear movements and the DNA damage response in the control of HIV infection by structural components of the nuclear envelope.

Introduction

Successful infection of cells by HIV requires an active transport of the virus through the physical barrier of the nuclear envelope. Nuclear entry of HIV is coordinated with the completion of reverse transcription and selection of integration sites (Dharan et al., 2020; Schaller et al., 2011). The capsid protein of HIV engages multiple interactions with nuclear pore complex (NPC) components and associated proteins such as Cyclophilin A to achieve this coordination (Yamashita and Engelman, 2017).

In the nuclear envelope, in addition to NPC proteins, SUN proteins located at the inner nuclear membrane impact HIV infection (Bhargava et al., 2018). SUN1 and SUN2 are integral proteins of the inner nuclear envelope of somatic cells. They play essential roles in the maintenance of genomic stability and the resolution of DNA damage (Lawrence et al., 2016; Lei et al., 2012). SUN proteins possess a lamin-binding domain at their N-terminus located in the nucleoplasm. Lamins are intermediated filament proteins that assemble the nuclear lamina, a dense meshwork contributing to mechanical protection, organization of chromatin domains and recruitment of DNA repair factors (Burke and Stewart, 2013; Gonzalo, 2014). At their C-terminus, SUN proteins interact with the KASH domains of nesprins in the perinuclear space. Nesprins are large integral proteins of the outer nuclear membrane (Burke and Stewart, 2013). Nesprins have multiple interactions with cytoskeletal proteins, enabling a dynamic anchoring of the nucleus within the cells.

SUN2 was first identified as an antiviral factor against HIV-1 in the context of a cDNA screen (Schoggins et al., 2011). Subsequent studies confirmed and extended the antiviral viral effect of SUN1 and SUN2 overexpression on HIV-1 and HIV-2 infection (Donahue et al., 2016; Lahaye et al., 2016; Luo et al., 2018; Schaller et al., 2017). SUN1 and SUN2 overexpression limits the level of HIV-1 nuclear import (Donahue et al., 2016; Luo et al., 2018; Schaller et al., 2017), leading to reduced viral integration. Furthermore, nanotubes of HIV-1 capsid and

nucleocapsid proteins produced *in vitro,* pull down SUN1 and SUN2 proteins from cell lysates, suggesting that SUN proteins and the viral capsid protein may interact directly or indirectly during infection (Schaller et al., 2017).

The role of endogenous SUN2 in HIV-1 infection has been examined but a consensus has not been reached (Donahue et al., 2017; Lahaye et al., 2016; Schaller et al., 2017; Sun et al., 2018). Three studies concurred with a requirement for SUN2 in HIV-1 infection in primary CD4+ T cells, in monocyte-derived dendritic cells and in THP-1 cells, although the strength of this requirement varies between cell type (Donahue et al., 2017; Lahaye et al., 2016; Schaller et al., 2017). A fourth study obtained contradicting results and proposed that endogenous SUN2 instead limits HIV infection at the level of viral promoter expression (Sun et al., 2018). We initially proposed that HIV infection requires an optimal level of SUN2 protein, and that both depletion and overexpression impair infection, not necessarily through the same mechanism (Lahaye et al., 2016). This notion fits well with the structural role of the LINC complex in nuclear architecture. Of note, endogenous SUN2 level varies with the extent of T cell activation (Sun et al., 2018). It is thus conceivable that variable experimental conditions between studies, particularly using sensitive primary immune cells, could account for the variable effects of endogenous SUN2 on HIV infection. SUN2 is also implicated in the effects of Cyclophilin A (CypA) on HIV-1 infection. In HeLa cells, SUN2 overexpression abrogates the sensitivity of HIV-1 capsid mutant N74D to Cyclophilin A inhibition (Lahaye et al., 2016). In primary CD4+ T cells and murine bone-marrow derived dendritic cells, endogenous SUN2 is required for the Cyclophilin A-dependent steps of HIV infection (Lahaye et al., 2016). Another study however, did not observe this effect in primary CD4+ T cells (Donahue et al., 2017). These differences may reflect the use of different read-outs for quantifying the impact of cyclophilin A inhibition on infection.

Our understanding of the antiviral effect of SUN1 is less advanced. In HEK293A cells, the antiviral effect of SUN1 overexpression requires the interaction of Cyclophilin A with HIV-1 capsid protein (Luo et al., 2018). In THP-1 cells, endogenous SUN1 is not required for HIV-1 infection (Schaller et al., 2017).

The strong antiviral effect of SUN protein overexpression on HIV infection exploits one or several points of weakness in the viral replication cycle. The cellular mechanisms by which elevated levels of SUN expression block HIV infection are not known. Intriguingly, SUN2 overexpression is associated with alteration of nuclear envelope shape, suggesting that SUN might interfere with HIV infection through a perturbation of the integrity of the nucleus (Donahue et al., 2016; Lahaye et al., 2016). However, it has not been possible so far to explain how SUN proteins are perturbing cellular and nuclear physiology to impact HIV.

Results

SUN1 and SUN2 proteins demonstrate HIV strain-specific antiviral effects

To gain insights in SUN1- and SUN2-mediated antiviral effects on the early steps of HIV infection, we first performed a comparative assessment of the antiviral effect of SUN1 and SUN2 on HIV infection in primary cells. To this end, we overexpressed SUN1 and SUN2 in primary monocyte-derived macrophages (MDMs) using lentiviral vectors (**Figure 1A**). In order to focus on the early phase of infection, cells were infected using single-round HIV-1 and HIV-2 encoding GFP in the place of the Nef gene. SUN1 and SUN2 induced an antiviral effect on HIV-1 and HIV-2 (**Figure 1B**). Unexpectedly, SUN1 and SUN2 did not show an identical antiviral effect on the two strains. The calculation of the ratio of inhibition by SUN1 over SUN2 revealed that HIV-1 was preferentially inhibited by SUN1, while HIV-2 was preferentially inhibited by SUN2 (**Figure 1B**). In MDMs, HIV-1 infection is sensitive to inhibition by Cyclosporin A (CsA). CsA treatment did not further inhibit infection in cells overexpressing SUN1 or SUN2 (**Figure 1B**). We analyzed the progression of HIV-1 and HIV-2 infection in the context of SUN protein expression using RT-qPCR on viral DNA species. For HIV-1, both SUN1 and SUN2 overexpression reduced the level of integrated viral DNA (**Figure 1C**). However, SUN1 reduced the total amount of viral DNA, while SUN2 reduced the level of 2-LTR circles, that are a hallmark of viral entry into the nucleus. CsA reduced the total amount of viral DNA in control cells and there was no additional reduction following SUN protein expression. For HIV-2, SUN1 and SUN2 significantly reduced 2-LTR circles only. These experiments indicate that SUN1 and SUN2 have strain-specific antiviral effects and that they modify different steps of viral infection.

We similarly overexpressed SUN1 and SUN2 in HeLa cells (**Figure 1D**). SUN1 overexpression had a greater inhibitory effect on HIV-1 infection than SUN2 overexpression, whereas in HIV-2 infection, SUN2 overexpression had a greater effect than SUN1, recapitulating the results

obtained in MDMs (**Figure 1E, 1F**). In HeLa cells, wild-type HIV-1 is not sensitive to CsA, but HIV-1 CA N74D is, similar to HIV-1 WT in MDM (De Iaco and Luban, 2014). We thus used this mutant to address the relationship between the antiviral effect of SUN and CsA sensitivity. Both SUN1 and SUN2 abolished CsA sensitivity of HIV-1 CA N74D in HeLa cells (**Figure 1G, 1H**). We next measured the levels of HIV-1 DNA species. SUN1 and SUN2 reduced the levels of integrated HIV-1 DNA and this effect was more pronounced for SUN1 (**Figure S1A**). Similar to MDM, SUN1 significantly inhibited the level of total viral DNA while the levels of 2-LTR circles were not significantly reduced. In contrast, SUN2 did not impact the level of total viral DNA but reduced the level of 2-LTR circles. We thus focused on HeLa cells for additional experiments aiming at characterizing the strain-specific inhibition of SUN1 and SUN2.

Strain-specific antiviral activity maps to the nucleoplasmic domain of SUN proteins

Cell-cell communication factors of innate immunity, such as interferons and cGAMP, can contribute to antiviral effects on top of cell-intrinsic restriction factors. Using a co-culture of SUN1/2-expressing cells and control cells expressing a fluorescent marker (TagRFP657), we found that the strain-specific effect of SUN1 and SUN2 on HIV-1 and HIV-2 infection is entirely cell-intrinsic in HeLa cells (**Figure 2A**). To determine if SUN1 and SUN2 induced an antiviral state at the cell-intrinsic level through expression of other antiviral genes, we performed a transcriptomic analysis of SUN1 and SUN2 overexpressing cells. Strikingly, we could not detect any differentially expressed gene in this dataset, aside from SUN1 and SUN2 themselves (**Figure S1B**). Next, we generated chimeras between SUN1 and SUN2 to map the strain-specific antiviral effect (**Figure 2B, 2C**). We found that the N-terminal nucleoplasmic domains of SUN1 and SUN2 confer strain-specificity (**Figure 2D, 2E**). These results establish

153 that SUN1 and SUN2 exert a cell-intrinsic HIV-strain specific antiviral effect on HIV infection,
154 that maps to the nucleoplasmic domain of SUN proteins.
155
156 **Antiviral effect of SUN proteins at the nuclear envelope**
157 We next sought to study how SUN1 and SUN2 impact cells to inhibit HIV infection. Electron
158 microscopy analysis revealed that both SUN1 and SUN2 overexpression induced deep
159 invaginations of the nuclear envelope, that appeared more pronounced with SUN2 (**Figure 3A**).
160 This raised the possibility that alteration of the shape of the nucleus could be responsible for
161 the antiviral effect. To test this, we asked if the antiviral effect of SUN occurs at the nuclear
162 envelope or whether it is the result of cytosolic accumulation of SUN proteins. SUN proteins
163 form the LINC complex with nesprins at the nuclear envelope by interaction with their KASH
164 domain within the perinuclear space. Expression of the isolated KASH domain (spectrin repeat-
165 KASH, SR-KASH) functions as a dominant negative by disrupting the SUN-Nesprin
166 interaction and displacing Nesprins from the nuclear envelope (Starr et al., 2003). We co-
167 expressed SR-KASH with SUN proteins (**Figure 3B**). We found that co-expression of the SR-
168 KASH construct partially rescued the antiviral effect on SUN1 and SUN2 on HIV-1 infection
169 (**Figure 3C**). These results support the notion that SUN proteins have an antiviral activity at
170 the nuclear envelope.
171
172 **Interplay between SUN proteins, HIV infection and the DNA damage response**
173 As a next step, we attempted to characterize the cellular processes affected by elevated levels
174 of SUN proteins. SUN1 and SUN2 are required to limit the accumulation of DNA damage in
175 cells (Lei et al., 2012). Since HIV infection is a DNA-damaging event, we considered the
176 possible interplay between SUN proteins, HIV infection and the DNA damage response. We
177 examined the level of γH2AX, an early marker of the DNA damage response. At baseline, we

did not detect any modification of γH2AX levels upon SUN1 or SUN2 expression (**Figure 4A, 4B**). To induce DNA damage, we selected etoposide, a topo-isomerase II inhibitor. Interestingly, SUN1 overexpression but not SUN2, significantly limited the levels of induced γH2AX after etoposide treatment (**Figure 4A, 4B**). To explore the potential link between DNA damage and infection, we infected HeLa cells in the presence of etoposide for the first 4 hours of the experiment. However, etoposide gradually induces apoptosis of treated cells (Rello-Varona et al., 2006), which hampered our ability to detect viable cells to measure infection after 48 hours. To circumvent this, we cultured cells in the presence of the caspase inhibitor Q-VD-Oph and lower doses of etoposide. Q-VD-Oph did not prevent γH2AX induction by etoposide treatment (**Figure 4C**). Etoposide treatment increased HIV-1 infection by 2-fold on average (**Figure 4D**). HIV-2 infection was also increased but significantly at only one dose of etoposide tested, with a smaller fold change. Next, we combined SUN expression with etoposide to determine the epistatic relationship between DNA damage induction and SUN expression on the level of HIV infection. Here, we used a higher MOI to observe the antiviral effect of SUN proteins. The increase induced by etoposide treatment on control cells was consistently observed across experiments. Interestingly, SUN1 abrogated the proviral effect of etoposide treatment and in sharp contrast, etoposide treatment rescued cells from the antiviral effect of SUN2 (**Figure 4E, 4F**). Thus, SUN1 overexpression, which restricts HIV-1 infection more than SUN2, operates downstream of DNA damage induction, while SUN2 overexpression impacts infection upstream of DNA damage.

DNA damage induction by ATR inhibition and role of HIV-1 Vpr

Next, we looked for a different approach to induce DNA damage that would be functionally linked to the nuclear envelope. ATR is a DNA damage sensor and functions as a checkpoint at the nuclear envelope in response to mechanical stress (Kumar et al., 2014). ATR inhibition

heightens DNA damage in cells (Foote et al., 2018). Furthermore, in HIV-1, expression of the accessory protein Vpr causes DNA damage and activates ATR (Roshal et al., 2003), although the relevance of this effect in the context of virion-packaged Vpr is unknown. Considering the significance of ATR at the nuclear envelope and its relationship with Vpr, we asked if DNA damage induction by ATR inhibition, SUN and Vpr are functionally related. We inhibited ATR using AZD6738, a next-generation inhibitor with improved specificity (Foote et al., 2018). As expected, ATR inhibition increased the levels of γH2AX in HeLa cells (**Figure 5A**). We next infected HeLa cells with p24-normalized and sucrose-cushion purified stocks of the HIV-1 single-round virus and its HIV-1 vpr-deficient (vpr-) counterpart. ATR inhibition increased vpr-positive HIV-1 infection in HeLa cells by 2-fold, similar to etoposide treatment (**Figure 5B, left panel**). Concomitant SUN protein overexpression inhibited HIV-1 infection and abrogated the proviral effect of ATR inhibition, again similar to the etoposide treatment. Unexpectedly, the titer of the p24-normalized HIV-1 vpr- was slightly higher than the HIV-1 wild-type counterpart in HeLa cells, and HIV-1 vpr- was insensitive to ATRi (**Figure 5B, right panel**). However, HIV-1 vpr- remained fully sensitive to the antiviral effect of SUN protein expression. In sum, this data supports the idea that increased DNA damage favors HIV-1 infection of HeLa cells and that SUN1 operates downstream of this to block infection. Intriguingly, this data also revealed that sensitivity to ATR inhibition is a HIV-1 vpr phenotype in single-round infection of HeLa cells.

Endogenous Lamin A/C limits HIV-1 infection in HeLa cells

We sought to further explore the relationship between infection, DNA damage and structure of the nuclear envelope. We searched for an orthogonal approach to perturb the nuclear envelope structure and the DNA damage response. Lamin A/C expression is required to maintain a regular nuclear shape (Lammerding et al., 2004) and to protect from DNA damage (Singh et

al., 2013). We used short-hairpin RNA to reduce expression of Lamin A/C (**Figure 6A**). Similar to SUN protein overexpression, knock-down of Lamin A/C compromised the regularity of the nuclear envelope shape (**Figure 6B**). To quantify this effect, we measured the shape descriptor 'solidity' of the nucleus: solidity values close to 1 indicate smoothly convex nuclei while lower values correspond to deformed, lobulated nuclei, presenting concave invaginations. Overexpression of SUN proteins and silencing of lamin A/C increased nuclear envelope deformation, although this effect was less pronounced in cells overexpressing SUN1 (**Figure 6C**). The endogenous levels of Lamin A/C and SUN proteins were not reciprocally affected by SUN overexpression or Lamin A/C silencing. (**Figure 6A**). After infection, Lamin A/C knock-down unexpectedly increased HIV-1 infection levels by 1.6-fold, while HIV-2 infection was not affected (**Figure 6D**). Lamin A/C thus limits HIV-1 infection in HeLa cells. However, the increase in nuclear envelope shape irregularities does not explain how lamin A/C depletion and SUN protein overexpression affect HIV infection. Given the opposing effects of SUN overexpression and Lamin A/C knock-down on HIV-1 infection, we examined if the antiviral effect of SUN proteins requires endogenous lamins. We knocked-down Lamin A/C, Lamin B1 and Lamin B2 and co-expressed SUN proteins (**Figure 6E**). Viable Lamin B1-depleted HeLa cells could not be maintained in culture. Lamin A/C depletion enhanced HIV-1 infection as above, and Lamin B2 depletion had no effect (**Figure 6F**). SUN proteins maintained their antiviral effect irrespective of the level of Lamin A/C and Lamin B2. This shows that the effect of elevated levels of SUN proteins is dominant on the effect of Lamin A/C depletion on HIV-1 infection.

Next, we examined the level of γH2AX after etoposide treatment and Lamin A/C depletion. Treatment with a high dose of etoposide (500 μM) for 24 hours induced an increase of γH2AX level in wild-type HeLa cells, while a lower dose (50 μM) had no impact at this time point (**Figure 6G**). In the absence of Lamin A/C, HeLa cells became hyper-sensitive to etoposide

253 treatment (**Figure 6G**). Thus, the increase in HIV-1 infection observed after Lamin A/C
254 depletion correlates with an increased sensitivity to DNA damage. Altogether, these results
255 establish a functional correlation between the effect of SUN protein and endogenous Lamin
256 A/C on HIV-1 infection and on the cellular response to DNA damage induced by an exogenous
257 compound.
258
259 **Elevated SUN proteins do not alter NPC density, passive import or cell stiffness**
260 We next sought to identify the mechanisms that delineate the effects of elevated SUN proteins
261 and endogenous Lamin A/C depletion on infection. We characterized biophysical and structural
262 parameters in SUN-expressing cells. HIV-1 enters the nucleus through NPCs. We labelled
263 NPCs using a marker of Nup153 on tangential confocal microscopy sections of the nuclear
264 envelope (**Figure S2A**). Overexpression of SUN proteins did not alter NPC density at the
265 nuclear envelope (**Figure S2B**). To determine if the NPC functionality was impaired by SUN
266 protein overexpression, we measured passive diffusion through the NPC using a Fluorescence
267 Recovery After Photobleaching (FRAP) assay on ubiquitous GFP. SUN proteins had no impact
268 on the rate of recovery of nuclear GFP (**Figure S2C, Movie 1**). Lamin A/C depletion reduces
269 stiffness of the nuclear envelope, resulting in a more deformable nucleus (Lammerding et al.,
270 2004). To determine if SUN proteins expression induced the opposite to match the effects on
271 infection, we measured the viscoelastic properties of the nuclei using a microfluidic
272 micropipette assay (Davidson et al., 2019). While we confirmed that Lamin A/C depleted cells
273 are more deformable, expression of SUN proteins had no impact on nuclear deformability
274 (**Figure S2D**).
275
276 **HIV-1 infection requires movement of the chromatin**

Next, we turned our attention to the endogenous state of chromatin. We performed live-imaging of cells with a DNA stain after SUN overexpression or Lamin A/C depletion. We observed that SUN1 and SUN2 overexpression appeared to lock the nucleus in place, while nuclei of Lamin A/C-depleted cells appeared highly dynamic (**Figure 7A, Movies 2–6**). We first asked whether the extent of chromatin movement inside the nuclei was altered. We isolated movies of single nuclei and performed a registration step to normalize X-Y positions and angle, therefore suppressing general nuclei displacement and rotation. We next measured chromatin movement in the registered nuclei by performing a particle image velocimetry (PIV) analysis. Strikingly, SUN1 and SUN2 overexpression reduced the displacement of chromatin over time and this effect was more pronounced with SUN1, while Lamin A/C depletion had the converse effect (**Figure 7B, S3A**). HeLa cells also exhibit seemingly random rotation of their nuclei, at various speeds and frequencies. Using the same dataset, we measured the rotation of the whole nucleus relative to the cytoplasm. We corrected the translational displacement of nuclei by registration and measured the angle of rotation over time using a custom-made analysis script (**Movie 7**). SUN1 and SUN2 reduced the average speed of nuclear rotation and the fraction of time spent rotating above a threshold of 1° (**Figure 7C, S3B**). The rotation of Lamin A/C-depleted nuclei was visibly higher than controls, but could not be reliably quantified due to the high levels of chromatin displacement that hampered the ability to set reference points. Overall, these results indicate that the impact of SUN and Lamin A/C proteins on HIV-1 infection is associated with the movement of chromatin within the cells.

Discussion

Our findings reveal that SUN1 and SUN2, though paralogs, have distinct effects on HIV infection. SUN1 overexpression is more efficient at inhibiting HIV-1 than SUN2. Meanwhile, SUN2 overexpression shows a marked antiviral activity against HIV-2. An analysis of the viral step impacted by these two proteins also reveals a discrepancy: while both SUN1 and SUN2 overexpression reduces the level of integrated HIV-1 DNA, SUN1 also inhibits total viral DNA amount while SUN2 reduces the levels of 2-LTR circles, a hallmark of nuclear entry. We also reveal that SUN1 and SUN2 differ in their response to DNA damage and its impact on HIV infection. SUN1 limits the response to etoposide as measured by the levels of γH2AX, while SUN2 enhances it. Strikingly, etoposide largely rescues the antiviral effect of SUN2 overexpression on HIV-1, while SUN1 is resistant to this effect. This result suggests that SUN1 and SUN2 may differ in the ways in which they establish interactions and functions within the nucleus, in line with previously reports showing non-redundant effects of SUN1 and SUN2 (Lei et al., 2009; Liu et al., 2007; Zhu et al., 2017)

Etoposide treatment also enhances the infection by HIV-1 by two-fold in HeLa cells in the absence of SUN protein overexpression, while HIV-2 is largely unaffected. Such a proviral effect of DNA damage has been previously observed in conditions of integrase inhibition (Ebina et al., 2012; Koyama et al., 2013). In contrast, it was previously reported that etoposide treatment inhibits HIV-1 infection in monocyte-derived macrophages (Mlcochova et al., 2018). We speculate that this is explained by the presence of a SAMHD1-dependent block in this cell type induced by etoposide in macrophages, but not in HeLa cells.

Similar to etoposide, ATR inhibition also enhances HIV-1 infection by 2-fold. The lack of requirement for ATR in HIV infection is consistent with prior studies (Ariumi et al., 2005; DeHart et al., 2005). Interestingly, the effect of ATR inhibition requires the presence of the Vpr gene in HIV-1. As a virus-encoded gene, Vpr has be shown to induce an ATR-dependent G2

arrest of the cell cycle (Zimmerman et al., 2006). Using purified and p24-normalized virus preparations, we made the unexpected observation that the Vpr-deficient virus is actually as infectious as the wild-type virus stimulated with ATR inhibition. In other words, in this asynchronous system of single-round infection of HeLa cells, the presence of the Vpr gene appears to provide a counter-intuitive two-fold reduction in infectivity of the virus, which is alleviated by ATR inhibition. However, Vpr has been associated with an enhanced expression for the viral LTR during G2 arrest (Goh et al., 1998). We speculate that in terms of viral replicative fitness, the reduction in single-round infectivity entailed by Vpr is cancelled out by this proviral effect of Vpr during G2 arrest. Of note, both SUN1 and SUN2 overexpression inhibit HIV-1 infection irrespective of ATR inhibition. In contrast, etoposide rescues the antiviral effect of SUN2 on HIV-1, raising the possibility that ATR itself might play a role in the rescue of the SUN2 antiviral effect.

Multiple lines of evidence from our work indicate that the structure of the nuclear envelope impacts HIV infection. The ability of SR-KASH to partially rescue the antiviral effects of SUN proteins indicates that the LINC complex, which is located at the nuclear envelope, is involved. Despite the important morphological changes induced by SUN protein expression, we did not observe any change at the level of gene expression, suggesting that any SUN-mediated effect on the nucleus and, subsequently, on HIV infection is post-transcriptional. ATR is enriched at the nuclear envelope during S phase and upon mechanical stretching, two processes that increase nuclear envelope stress (Kumar et al., 2014). ATR-deficient cells exhibit deformed nuclei, reminiscent of Lamin A/C depletion or SUN protein overexpression (Kidiyoor et al., 2020). Vpr overexpression was previously shown to induce herniations of the nuclear envelope associated with defects in the nuclear lamina (de Noronha et al., 2001). We also find that endogenous Lamin A/C has an antiviral effect, in agreement with a previous study (Sun et al., 2018).

We examined several effects of SUN protein overexpression and endogenous Lamin A/C on nuclear shape, deformability, NPC distribution and function and chromatin dynamics. The effects on HIV-1 infection match the effects of the proteins on chromatin dynamics: decreased HIV-1 infection is associated with a decreased chromatin motility inside the nucleus and with decreased rotation of the nucleus relative to the cytoplasm. In contrast, HIV-2 infection is more susceptible to SUN2 than SUN1 and is not affected by Lamin A/C depletion. Overexpression of SUN2 deforms nuclei more than SUN1 but internal chromatin dynamics and nuclear rotation are less impacted. This strain specificity could be linked to a different dependency on host factors between HIV-1 and HIV-2 (Braaten and Luban, 2001). SUN and Lamin proteins have been previously linked to chromatin mobility and nuclear rotation (Ji et al., 2007; Lottersberger et al., 2015; Oza et al., 2009; Ranade et al., 2019). Interestingly, nuclear rotation is required for optimal infection by another nuclear-invading virus, HCMV (Procter et al., 2018). This rotation is required to promote spatial chromatin segregation that favors viral gene expression (Procter et al., 2018). We propose that HIV-1 infection requires nuclear rotation and chromatin movements for optimal integration and subsequent viral expression.

Our results highlight the interplay between HIV infection, structural proteins of the nuclear envelope and the DNA damage response. Nuclear rotation and chromatin dynamics emerge as potentially important factors that control HIV infection. Future studies will be required to address the underlying molecular mechanisms, which we anticipate will require the use of biophysical approaches. It will also be important to examine these mechanisms in the frame of the diversity of lentiviruses and their relevance for viral replication and innate immune sensing mechanisms in primary target cells.

Acknowledgments

We thank N. De Silva for setting up the γH2AX intranuclear staining; V. Teixeira Rodrigues for assistance with primary macrophages; P. Benaroch for critically reading this manuscript; M. Piel, N. De Silva, N. Jeremiah and A. Williart for discussions. We acknowledge the PICT-IBiSA imaging facility, member of the France-BioImaging national research infrastructure, supported by the CelTisPhyBio Labex (ANR-10-LBX-0038) part of the IDEX PSL (ANR-10-IDEX-0001-02 PSL), and Audrey Rapinat and David Gentien from the Genomics Platform at Institut Curie. This work was supported by Institut Curie, INSERM, and by grants from the Agence Nationale de la Recherche (ANR-10-IDEX-0001-02 PSL, ANR-11-LABX-0043, ANR-17-CE15-0025-01, ANR-19-CE15-0018-01, ANR-18-CE92-0022-01, France-BioImaging ANR-10-INSB-04), the Agence Nationale de la Recherche sur le SIDA (ECTZ36691, ECTZ25472, ECTZ71745), Sidaction (VIH2016126002, 17-1-AAE-11097-2). AB was supported by fellowships from PSL University and Fondation pour la Recherche Médicale, grant number 8250. PMD was supported by fellowships from La Ligue contre le Cancer (REMX17751) and Fondation ARC (PDF20161205227).

Figure Legends

Figure 1 Distinct antiviral activities of SUN1 and SUN2 against HIV-1 and HIV-2

(A) Detection of SUN1, SUN2 and actin in MDMs transduced with mTagBFP-2A control, SUN1 or SUN2 lentivectors (representative of n = 3).

(B) Left, viral titers as infectious units (i.u.) per mL based on percentages of GFP^+ MDMs 48 hours after infection with serial dilutions of HIV-1 or HIV-2 encoding GFP in Nef and pseudotyped with VSV-G, with or without 2 µM CsA (n = 9 donors, paired RM ANOVA one-way on Log-transformed titers with Sidak post-test, line at mean). Right, ratios of titer fold changes (FC) control over SUN1 (SUN1 FC) or control over SUN2 (SUN2 FC) (paired t-test, line at mean).

(C) Detection of HIV-1 total DNA, 2-LTR circles DNA and integrated DNA by RT-qPCR at 24 hours after infection with HIV-1 or HIV-2 (dilution factor: 0.17) of MDMs transduced with mTagBFP-2A control, SUN1 or SUN2 lentivectors. Reverse transcriptase inhibitors Azidothymidine (AZT; 24 µM) and Nevirapine (NVP; 10 µM) were added during infection only on control cells (n=4 donors, paired RM ANOVA one-way with Sidak post-test, line at mean ± SEM).

(D) Detection of SUN1, SUN2 and actin in HeLa cells transduced with mTagBFP-2A control, SUN1 or SUN2 lentivectors.

(E) GFP expression in BFP-positive HeLa cells transduced with mTagBFP-2A control, SUN1 or SUN2 lentivectors, 48 hours after infection with indicated dilutions of HIV-1 and HIV-2 (representative data from one experiment at the indicated dose of virus).

(F) Left, Viral titers based on percentages of GFP^+ cells after infection with serial dilutions of virus as in **(E)** (n = 6, paired RM ANOVA one-way on Log-transformed titers, with Dunnet's post-test, line at mean). Right, ratios calculated as in **(B)**.

(G) Percentage of GFP^+ in BFP^+ HeLa cells transduced with mTagBFP-2A control, SUN1 or SUN2 lentivectors, 48 hours after infection with serial dilutions of HIV-1 or HIV-1 CA N74D, with or without treatment with 2 µM of CsA (n = 3 independent experiments).

(H) Viral titers as in (G) (n = 3, paired RM ANOVA one-way on Log-transformed titers with Sidak's post-test, line at mean).

Ctrl = control, $^{*}p < 0.05$, $^{***}p < 0.001$, $^{****}p < 0.0001$; ns, not statistically significant.

Figure 2 Mapping of the strain-specific antiviral activity of SUN proteins

(A) mTagBFP-2A Ctrl, mTagBFP-2A-SUN1 and mTagBFP-2A-SUN2 expressing HeLa cells were co-cultured at a 1:1 ratio with HeLa cells expressing TagRFP657-2A and infected with serial dilutions of HIV-1 and HIV-2. Titers were calculated based on percentage of GFP^+ cells 48 hours post-infection dilutions within the indicated populations (n=3 independent experiments, paired RM ANOVA one-way on Log-transformed titers with Sidak's post-test, line at mean).

(B) Schematic representation of chimeric proteins between full-length SUN1 (red) and SUN2 (blue). Amino-acid residues retained in hybrid proteins are indicated within brackets.

(C) Detection of SUN1, SUN2 and actin in HeLa cells transduced with the indicated mTagBFP-2A lentivectors. Two antibodies targeting SUN2 that recognize different epitopes within the protein were used.

(D) Percentage of GFP^+ in BFP^+ HeLa cells transduced with the indicated mTagBFP-2A lentivectors, 48 hours after infection with serial dilutions of HIV-1 or HIV-2 (n=3 independent experiments).

(E) Viral titers based on percentages of GFP^+ cells shown in **(D)** (n=3, paired RM ANOVA one-way with Sidak's post-test, line at mean).

Ctrl = control, $^{*}p < 0.05$, $^{**}p < 0.01$, $^{***}p < 0.001$, $^{****}p < 0.0001$; ns, not statistically significant.

Figure 3 SUN proteins inhibit HIV infection at the nuclear envelope

(A) Representative electron micrograph showing nuclei in control, SUN1 and SUN2 overexpressing HeLa cells (scale: 10, 2 and 5 µm respectively).

(B) Detection of SUN1, SUN2, GFP and actin in HeLa cells transduced with TagRFP657-expressing control, SUN1 or SUN2 lentivectors, combined with control GFP or SR-KASH DN fused to GFP expressing lentivectors. The same lysates were loaded onto two separate membranes, the housekeeping control is shown for both.

(C) Top, percentage of BFP^+ within $tagRFP657^+$ HeLa cells 48 hours after infection with serial dilutions of HIV-1 encoding BFP in the place of Nef, pseudotyped with VSV-G. Bottom, viral titers based on percentages of BFP^+ cells (n=3, paired RM ANOVA one-way on Log-transformed titers, with Sidak's post-test, line at mean ± SEM).

Ctrl = control, $^{*}p < 0.05$, $^{**}p < 0.01$, $^{***}p < 0.001$; ns, not statistically significant.

Figure 4 Interplay between HIV-1 infection, SUN protein and the DNA damage response

(A) Viability and γH2AX intracellular staining in HeLa cells transduced with mTagBFP-2A control, SUN1 or SUN2 lentivector, 24 hours after treatment with 500 µM of etoposide or 1% DMSO as control (representative experiment from n = 3).

(B) Quantification of $γH2AX^+$ HeLa cells treated as in **(A)** (n=4, paired RM ANOVA one-way with Sidak's post-test, line at mean).

(C) Quantification of $γH2AX^+$ HeLa cells 24 hours after a 4-hour treatment with 5 µM, 50 µM etoposide or corresponding DMSO control. 50 µM of Q-VD-Oph were present throughout the experiment (n=3, paired RM ANOVA one-way with Sidak's post-test, line at mean ± SEM).

(D) Top, percentage of GFP^+ HeLa cells 48 hours after infection with two dilutions of HIV-1 or HIV-2, treated as in **(C)**. Cells were treated and infected simultaneously, the drugs and the

virus were washed out at 4 hours post-treatment/infection. 50 µM of Q-VD-Oph were maintained throughout the experiment. Bottom, viral titers based on percentages of GFP^+ cells (n=3, paired RM ANOVA one-way with Sidak's post-test, line at mean).

(E) Quantification of $\gamma H2AX^+$ HeLa cells, transduced with mTagBFP-2A control, SUN1 or SUN2 lentivectors, 4 hours after treatment with 50 µM of etoposide or corresponding DMSO control (n=3, paired RM ANOVA one-way with Sidak's post-test, line at mean ± SEM).

(F) Left, percentage of GFP^+ cells in BFP^+ HeLa cells expressing control, SUN1, SUN2 lentivectors and treated as in **(E)**, 48 hours after infection with purified HIV-1 env-nef-, expressing GFP in the place of Nef and pseudotyped with VSV-G. Right, GFP+ percentages at viral dilution 0.02 (n=3, experimental pairs are indicated; RM ANOVA two-way test, uncorrected Fischer' LSD). 50 µM of Q-VD-Oph were maintained throughout the experiment. Ctrl = control, hpt = hours post treatment, $^*p < 0.05$, $^{**}p < 0.01$, $^{***}p < 0.001$, $^{****}p < 0.0001$; ns, not statistically significant.

Figure 5 DNA damage induction by ATR inhibition stimulates HIV-1 infection in a Vpr-dependent manner

(A) Top, γH2AX intracellular staining in mTagBFP-2A control HeLa cell line, 24 hours after treatment with either 1 µM of AZD6738 or 0.01% DMSO (representative experiment). Bottom, quantification of specific γH2AX staining as geometric mean fluorescence intensity (GeoMFI) of the antibody signal divided by the GeoMFI of the isotype control (n=4, paired t-test, $^*p < 0.05$, line at mean ± SEM).

(B) Viral titers based on percentages of GFP^+ cells, within BFP^+ HeLa cells expressing Ctrl, SUN1 or SUN2 lentivector, with or without treatment with 1 µM of AZ6738, 48 hours after infection with serial dilutions of purified, p24-normalized, HIV-1 env-nef- or HIV-1 env-nef-

vpr- encoding GFP in the place of Nef, pseudotyped with VSV-G (n=3, paired RM ANOVA one-way with Sidak's post-test, line at mean ± SEM).

Ctrl = control, hpt = hours post treatment, $^{*}p < 0.05$, $^{***}p < 0.001$, ns, not statistically significant.

Figure 6 Interplay between HIV-1 infection, Lamin A/C protein and the DNA damage response

(A) Detection of SUN1, SUN2, Lamin A/C and actin in HeLa cells transduced with mTagBFP-2A control, SUN1 or SUN2 lentivectors, negative control LacZ (shLACZ) or lamin A/C (shLMNA) targeting shRNA-encoding lentivectors.

(B) Nuclei of HeLa cells lines as in (A) visualized on fixed cells using SiR-DNA dye. Images show signal from an individual, central confocal plane, scale bar is at 10 µm.

(C) Solidity index of nuclei as in **(B)**. Legend indicates total number of nuclei analyzed per cell line (representative of n=2 experiments, one on fixed cells and one with live imaging). Unpaired ANOVA one-way with Sidak's, line at median.

(D) Viral titers based on percentages of GFP^{+} HeLa cells lines from **(A)** after infection with serial dilutions of HIV-1 and HIV-2 (n=3, paired RM ANOVA one-way with Sidak's post-test, line at mean).

(E) Detection of SUN1, SUN2, Lamin A/C, Lamin B2 and actin in HeLa cells co-transduced with mTagBFP-2A control, SUN1 or SUN2 lentivectors and with LacZ, lamin A/C or lamin B2 (shLMNB2) targeting shRNA-encoding lentivectors.

(F) Viral titers based on percentages of GFP^{+} HeLa cells as shown in **(E)** after infection with serial dilutions of HIV-1 and HIV-2 (n=3, paired RM ANOVA one-way with Sidak's post-test, line at mean).

(G) Quantification of $\gamma H2AX^+$ HeLa cells transduced with either a LacZ or lamin A/C targeting shRNA lentivector, 24 hours after treatment with indicated doses of etoposide or DMSO control (n=3, line at mean ± SEM).

Ctrl = control, hpt = hours post treatment, $^{*}p < 0.05$, $^{**}p < 0.001$, $^{***}p < 0.001$, $^{****}p < 0.0001$; ns, not statistically significant.

Figure 7 SUN protein overexpression and endogenous Lamin A/C limit movements of the chromatin

(A) Particle Image Velocimetry (PIV)–of DNA within nuclei of HeLa cells transduced with mTagBFP-2A control, SUN1 or SUN2 lentivectors, negative control LacZ or lamin A/C targeting shRNA-encoding lentivectors. PIV is shown for individual representative nuclei of each cell line, top panels show overall flow and bottom panels show individual vectorial displacements between two consecutive frames corresponding to two minutes of imaging. Scale bar corresponds to 5 µm. Reference color scale for pixel displacement per time frame is shown on left.

(B) Quantification of DNA displacement as µm/min from images as in **(A)**. Results are shown for one experiment from n = 2. Left, unpaired ANOVA one-way with Sidak's post-test, line at mean. Right, unpaired student t-test, line at mean.

(C) Quantification of nuclear rotation speed as degrees/minute (top) and rotation duration as fraction of total time spent rotating over a threshold of 1° (bottom) in HeLa cells transduced with mTagBFP-2A control, SUN1 or SUN2 lentivectors and imaged as in **(A)**. Results are shown for one experiment from n = 2. Unpaired ANOVA one-way with Sidak's (top) or Turkey's (bottom) post-test, line at mean.

Ctrl = control, $^{*}p < 0.05$, $^{**}p < 0.01$, $^{****}p < 0.0001$; ns, not statistically significant.

537 **Supplemental Material**

538 **Figure S1 HIV-1 DNA quantification and gene expression analysis of SUN-overexpressing**
539 **cells**

540 **(A)** Detection of HIV-1 total DNA, 2-LTR circles DNA and integrated DNA by RT-qPCR at
541 24 hours after infection (dilution factor: 0.1) of HeLa cells transduced with mTagBFP-2A
542 control, SUN1 or SUN2 lentivectors. AZT (24 µM) was added during infection when indicated
543 (n=3, paired RM ANOVA one-way with Turkey's post-test, line at mean ± SEM).
544 **(B)** Differential gene expression in SUN1 (Left) and SUN2 (Right) overexpressing cells over
545 control cells (FC, fold change; FDR, false discovery rate). Overexpressed SUN2 was codon-
546 optimized, rendering it sub-optimal for probe-based detection.
547 Ctrl = control, $^{*}p < 0.05$, $^{**}p < 0.001$, $^{***}p < 0.001$; ns, not statistically significant.
548

549 **Figure S2 Analysis of NPC density, passive nuclear import and cellular stiffness of SUN-**
550 **overexpressing cells**

551 **(A)** Left, confocal imaging of NUP153 staining in HeLa cells. Right, blow-up or region of
552 interest and detection of individual of NPC (red) using "Find Maxima" function. A
553 representative nucleus of cells overexpressing mTagBFP-2A-SUN2 is shown.
554 **(B)** Quantification of NPC density per μm^2 in nuclei from HeLa cells transduced with
555 mTagBFP-2A control, SUN1 or SUN2 lentivectors, imaged and analyzed as in **(A)** (total
556 number of nuclei analyzed per cell line are indicted, n=1 experiment; un-paired ANOVA one-
557 way with Sidak's post-test, line at mean).
558 **(C)** Passive diffusion from the cytoplasm to the nucleus measured by FRAP, in HeLa cells
559 transduced with mTagBFP-2A control, SUN1 or SUN2 lentivectors and a lentivector encoding
560 GFP. Top, representative layout of a photobleached control HeLa cell: imaging starts at t = 0
561 after high intensity laser exposure and ends at t = 80 seconds, when fluorescence in the nucleus

has been recovered (scale bar: 5 µm). Bottom left: GFP intensity recovery over time (s). For each individual cell, the background intensity was subtracted and intensity was normalized to 0 at t0 after photobleaching while the max intensity reached during the course of each measurement was set to 1. Curves show mean and standard deviation per time point across indicated number of cells per condition. Bottom right, hillslopes for each cell were calculated via non-linear regression fit (total number of nuclei analyzed per cell line are indicated, n=1 experiment; un-paired ANOVA one-way with Dunnett's post-test, line at mean ± SEM).

(D) Measurement of nuclear deformability. Left, representative image showing tagBFP-2A-Ctrl HeLa cells stained with SiR-DNA and going through microchannels under externally-applied pressure. The green arrow indicates the elongation of SiR-DNA staining within the channel, which is measured over time as a readout for nuclear deformability. Right, quantification of nuclear deformability across HeLa cell lines described in **(6A)** over time (the number of nuclei measured per cell line is indicated within brackets, n = 3 independent experiments).

Ctrl = control, ns, not statistically significant.

Figure S3 SUN protein overexpression and endogenous Lamin A/C limit movements of the chromatin, second experiment.

(A) Quantification of DNA displacement as µm/min from images as in Figure 7B, second experiment. Top, unpaired ANOVA one-way with Sidak's post-test, line at mean. Bottom, unpaired student t-test, line at mean.

(B) Quantification of nuclear rotation speed as degrees/minute (top) and rotation duration as fraction of total time (bottom) spent rotating over a threshold of 1°, as in Figure 7C, second experiment. Unpaired ANOVA one-way with Sidak's (top) or Turkey's (bottom) post-test, line at mean.

587 Ctrl = control, $^{*}p < 0.05$, $^{*}p < 0.01$ $^{***}p < 0.001$, $^{****}p < 0.0001$; ns, not statistically significant.

588

589

590 **Movie 1 Passive diffusion from the cytoplasm to the nucleus measured by FRAP.**

591 Representative movie of a HeLa cell overexpressing mTagBFP-2A-Ctrl and ubiquitous GFP
592 lentivectors. Immediately prior to imaging, high intensity 488 nm laser was directed to a small
593 region within the nucleus to bleach the GFP signal within this compartment. Imaging of the
594 whole cell starts at t = 0 immediately after bleaching. Recovery of the GFP signal in the nucleus
595 is observed as GFP diffuses back in from the cytoplasm until equilibrium is obtained. One frame
596 was taken every 2 seconds.

597

598 **Movies 2 Quantification of chromatin dynamics in mTagBFP-2A-overexpressing control**
599 **HeLa cells.**

600 Chromatin dynamics assessed by PIV. The analysis was performed on live confocal imaging
601 of DNA staining using SiR-DNA. An image was taken every 2 minutes. The left panel shows
602 registration of the object (one nucleus) across 10 time frames while the right panel shows the
603 flow of pixel clusters (interrogation windows) within the object, across consecutive time
604 frames. Warmer colors indicate high levels of displacement while cold colors indicate more
605 static regions. Scale bar corresponds to 5 µm.

606

607 **Movie 3 Quantification of chromatin dynamics in mTagBFP-2A-SUN1-overexpressing**
608 **HeLa cells.**

609 Analysis was performed as for Movie 2.

610

Movie 4 Quantification of chromatin dynamics in mTagBFP-2A-SUN2-overexpressing HeLa cells.

Analysis was performed as for Movie 2.

Movie 5 Quantification of chromatin dynamics in HeLa cells expressing a control shRNA against LacZ.

Analysis was performed as for Movie 2.

Movie 6 Quantification of chromatin dynamics in HeLa cells expressing a shRNA against Lamin A/C.

Analysis was performed as for Movie 2.

Movie 7 Measurement of nuclear rotation in a HeLa cell.

The analysis was performed on live confocal imaging of DNA staining using SiR-DNA. An image was taken every 2 minutes, for a total duration of 60 minutes. The angle was measured in reference to an image containing 2 fixed points (one at the center and one on the edge of the nucleus). In this example, HeLa overexpressing mTagBFP-2A control are shown.

Materials and methods

Constructs

The plasmid constructs for lentiviral expression and HIV infection used in this study are listed in **Table 1**. pTRIP-SFFV-tagBFP-2A-SUN1 Dharmacon was generated by overlapping PCR cloning from commercially bought cDNA (MGC cDNA cloneID: 40148817) into pTRIP-SFFV-tagBFP-2A (Cerboni et al., 2017). pTRIP-SFFV-tagBFP-2A-ntSUN2 was generated by overlapping PCR mutagenesis from pLX304-SUN2 (Lahaye et al., 2016) into pTRIP-SFFV-tagBFP-2A with concomitant introduction of silent mutations that are not targeted by SUN2 shRNA 4 and 5 (respectively GAGCCTATTCAGACGTTTCACTTT to GAACCGATCCAAACTTTCCATTTC and AAGAGGAAATCCAGCAACATGAAG to AAACGCAAGAGTTCTAATATGAAA). pTRIP-SFFV-tagBFP-2A-SUN1 Dharmacon (1-298)-ntSUN2 (220-717) and pTRIP-SFFV-tagBFP-2A-ntSUN2 (1-219)-SUN1 Dharmacon (299-785) were generated by overlapping PCR cloning from the full-length constructs. pTRIP-SFFV-tagRFP657-2A-SUN1 and pTRIP-SFFV-tagRFP657-2A-ntSUN2 were generated via restriction enzyme digestion from the tagBFP expressing vectors and ligation into pTRIP-SFFV-TagRFP657-2A backbone. HIV-GFP env-nef- was generated by PCR-mediated insertion of the Vpr+Vif+Vpu+ cassette from NL4-3 into HIV-GFP (Manel et al., 2010). HIV-GFP env-nef-vpr- was generated by overlapping PCR mutagenesis from HIV-GFP env-nef-, introducing a frameshift mutation within *vpr,* after the codon corresponding to amino-acid I63 (gaattc to gaaTTAAttc). HIV-mTagBFP2 and HIV-2 ROD9 ΔenvΔnef mTagBFP2+ were obtained via overlapping PCR mutagenesis, replacing GFP with the mTagBFP from pTRIP-SFFV-mTagBFP-2A.

Cells

GHOST (GHOST X4R5), 293FT and HeLa cells were cultured in DMEM with Glutamax, 10% fetal bovine serum (FBS) (Corning), and penicillin-streptomycin (Gibco). Human peripheral blood mononuclear cells (PBMCs) were isolated from buffy coats from normal human donors (approved by the Institut National de la Santé et de la Recherche Médicale ethics committee) using Ficoll-Paque PLUS (GE). $CD14^+$ cells were isolated by a positive selection with anti-human CD14 magnetic beads (Miltenyi) from PBMCs. To obtain macrophages (MDMs), $CD14^+$ cells were cultured in RPMI with Glutamax, 5% FBS (Eurobio), 5% human serum (Sigma), Penicillin-Streptomycin, Gentamicin (50 µg/ml, GIBCO) and HEPES (GIBCO) in the presence of recombinant human M-CSF (Miltenyi) at 50 ng/ml. Fresh media was added at day 5 or 6, and cells were treated/infected at day 9, after detachment via incubation with StemPro Accutase Cell Dissociation Reagent (Gibco) for 30 minutes at 37°C. Drug treatments performed on cultured cells are listed in **Table 2**.

Virus production

Viral particles were produced by transfection of 293FT cells in 6-well plates with 3 µg DNA and 8 µl TransIT-293 Transfection Reagent (Mirus Bio) per well. For VSV-G pseudotyped SIVmac virus-like particles (VLPs), 0.4 µg CMV-VSVG and 2.6 µg $pSIV3^+$ was used. For VSV-G pseudotyped HIV-1 and HIV-2 GFP or BFP-reporter viruses, 0.4 µg CMV-VSVG and 2.6 µg HIV DNA was used. For overexpression or sh-RNA mediated knock-down, 0.4 µg CMV-VSVG, 1 µg psPAX2 and 1.6 µg of lentivector of interest were combined. One day after transfection, media was removed, cells were washed once, and 3 ml per well of RPMI medium with Glutamax, 10% FBS (Gibco), PenStrep (Gibco), 50µg/ml Gentamicin (Gibco) and 0.01 M HEPES (Gibco) were added. Viral supernatants were harvested 1 day later, filtered using 0.45 µm pore filters, used fresh or aliquoted and frozen at −80°C. When required, the virus was purified and concentrated on a 20% sucrose cushion in phosphate buffered saline (PBS) in Ultra

Clear Centrifuge tubes (Beckman Coulter), via ultracentrifugation at 4°C at 31,000 *x g* in a SW32Ti swinging bucket rotor (Beckman Coulter). Viral pellets were then resuspended in complete medium at a 100-fold concentration compared to crude. Viral titers were measured on GHOST cells (titration as previously described (Manel et al., 2010) or using HIV-1 p24 ELISA (XpressBio). ELISA absorbance acquisitions were acquired on a FLUOstar OPTIMA (BMG Labtech) and data were analyzed and exported to Excel with MARS Data Analysis Software (BMG Labtech).

Cell Transduction for protein overexpression or knockdown

HeLa cells were counted and seeded in 6-well plates on the day prior to transduction. Purified virus was added at a 2:1 volume ratio on medium containing protamine at a final concentration of 1 µg/ml. $CD14^+$ monocytes were seeded in 10-cm dishes in the presence of 50 ng/ml M-CSF to induce differentiation into macrophages and transduced with purified SIVmac VLPs and lentiviruses carrying vector of interest, mixed at a 1:1 ratio. Human serum was added at day 1 post transduction. Transductions of monocytes was performed in the presence of protamine at a final concentration of 1 µg/ml. HeLa cells were washed once in PBS and passaged at 48 hours post transduction with or without 2 µg/ml of puromycin. For MDMs, medium was replaced at day 5-6 post transduction. Overexpression was assessed by quantification of fluorescent reporter signal via flow cytometry on a BD FACSVerse flow cytometer. Both overexpression and protein knock-down were confirmed by Western Blotting at day of experiment.

Cell infection

HeLa, GHOST and MDMs (day 8-9 post transduction) were seeded and infected in the presence of 1 µg/ml of protamine with serial dilutions of frozen viral stocks in a BSL-3 laboratory. Virus was removed at 48 hours post-infection, cells were washed, harvested, stained for viability

using Fixable Viability Dye eFluor 780 in PBS where required, fixed in 1% paraformaldehyde (PFA; Electron Microscopy Sciences) and analyzed for GFP or BFP positivity via flow cytometry on a BD FACSVerse flow cytometer. Viral titers were calculated based on seeded cell number and the percentages of infected cells, within the linear range of infection.

HIV DNA quantification

HeLa cells and MDMs were infected as described, with the addition of infected wells treated with RT inhibitors as negative control. For this purpose, either 24 µM of AZT (Sigma) or 10 µM of NVP (Sigma) were used. After 24 hours, cells were washed in PBS and harvested. Total DNA was extracted from cell pellets using NucleoSpin Tissue (Macherey-Nagel) kit, as per manufacturer's protocol. Real-time PCR analysis was performed as previously described (Lahaye et al., 2013). Each sample was measured in triplicate for all primers. For beta-globin, primers were bglobin-f and bglobin-r. Cycling conditions were 1x 95°C for 5'; 35x 95°C for 10'', 65°C for 20'' (50°C for beta-globin) and 72°C for 30''. Relative concentrations of total DNA (Late RT), 2-LTR circles and integrated viral DNA were calculated relative to beta-globin using the ΔCt method. The primers used are listed in **Table 3**.

Western Blotting

0.5 to 1 million cells were lysed in 100 µL of RIPA buffer (50mM Tris HCl, 150mM NaCl, 0.1% SDS, 0.5% DOC, 1% NP-40, Protease inhibitor (Roche; 1187358001)). Lysis was performed on ice for 30'. Lysates were cleared by centrifugation at 8000 g for 8 minutes at 4°C, 20 µl of Laemmli 6x (12% SDS, 30% Glycerol, 0.375M Tris-HCl pH 6.8, 30% 2-mercaptoethanol, 1% bromophenol blue) was added and samples were boiled at 95°C for 15'. Cellular protein lysates were resolved on Criterion or 4%–20% Bio-Rad precast SDS-PAGE gels and transferred to PVDF membranes (Bio-Rad). Membranes were saturated and proteins

were blotted with antibodies in 5% non-fat dry milk, PBS 0.1% Tween buffer. ECL signal generated via Clarity Western ECL substrate (Bio-Rad) was recorded on the ChemiDoc-XRS or ChemiDoc Touch Bio-Rad Imager. Data was analyzed and quantified with the Image Lab software (Bio-Rad). The antibodies used in this study are listed in **Table 4**.

Live Confocal Imaging

For live imaging, HeLa cells were plated either in a glass bottom FluoroDish (World Precision Instruments) or in a glass-bottom Cellview Cell Culture Dish with 4 compartments (Greiner Bio-One), on the day prior to experiments. One hour before imaging, cells were incubated with 1 µM of SiR-DNA (Tebu Bio), directly in the culture medium, at 37°C. Images of cells were acquired with a Leica DmI8 inverted microscope equipped with an SP8 confocal unit using a 20x dry objective (NA=0.75, pixel size was fixed to 0.284 µm). Imaging was performed in an on-stage incubator chamber at 37°C, with 5% CO_2. An image per condition was taken every 2 minutes, unless specified otherwise.

Image analysis was performed using Fiji software (Schindelin et al., 2012). For chromatin dynamics analysis, a homemade macro was first used to do segmentation of each nucleus on the movie and identify them using the 3D object counter. Particle Image Velocimetry (PIV) analysis was then performed on SiR-DNA staining using the PIV plug-in (Tseng et al., 2012). PIV is a basic optic flow analysis, that divides each image of a stack in small clusters of pixels (interrogation windows) and measures the displacement of each cluster between pairs of consecutive frames. The cross-correlation then generates a pattern of "movements" within the nucleus that are color-coded based on the amplitude of the vector corresponding to the displacement of each cluster. An in-house script was used to first align each individual nucleus, then measure and average SiR-DNA displacements over the ten first time points. Red shades indicate higher amplitudes of displacement while violets correspond to quasi-immobile

753 clusters. For nuclear rotation analysis, a macro was used to measure rotation angles across the
754 first 30 frames. Briefly, individual nuclei were first aligned using a translation transformation
755 of the MultiStackReg plug-in (Brad Busse, Stanford), then they were aligned using the rotation
756 transformation and the transformation was applied to a reference image containing 2 fixed
757 points (one at the center and one on the edge) to measure the rotation. A threshold of 1
758 degree/minute was used to define rotating nuclei. The percentage of rotation time and the
759 average velocity was then computed.
760
761 Confocal Immunofluorescence Imaging
762 For immunofluorescence, HeLa cells were grown overnight onto 12 mm glass coverslips
763 (Thermo Scientific) placed in 6-well plates. Cells were fixed with 4% PFA for 20 minutes at
764 room temperature. Coverslips were washed multiple times with PBS and quenched with 0.1M
765 Glycine in PBS(Life Technologies) for 10 minutes at room temperature. Coverslips were then
766 blocked with PBS, 0.2% (w/v) bovine serum albumin (BSA) (Euromedex), 0.05% (w/v)
767 Saponin from quillaja bark (SIGMA) for 30 minutes at room temperature. Cells were stained
768 overnight with anti-NUP153 antibody at 2 µg/mL (1:50 dilution) or with Normal Rabbit IgG
769 Isotype Control at corresponding concentration of the primary antibody, in PBS, 0.2% (w/v)
770 BSA, 0.05% (w/v) Saponin + 10% goat serum (Sigma), at 4°C in a humidified chamber. The
771 following day, cells were washed multiple times and incubated with the secondary antibody
772 Alexa Fluor 546 goat anti-rabbit IgG (H+L) (Invitrogen; 1:200 dilution in PBS-BSA-Saponin)
773 in the presence of 1 µM of SiR-DNA for 2 hours in the dark, at room temperature. Coverslips
774 were washed multiple times in PBS-BSA-Saponin and finally rinsed once in distilled water.
775 Coverslips were mounted onto glass slides using Fluoromount G (eBioscience) mounting
776 medium. The slides were finally dried at 37°C for 1h and stored at 4°C. Cells were imaged with

a Leica DmI8 inverted microscope equipped with an SP8 confocal unit using an oil immersion 63x objective (NA=1.4) with applied Type F Immersion Liquid (Leica).

Fluorescence Recovery After Photobleaching

Cells were seeded at 2.5 x 10^5 cells/dish in a glass bottom FuoroDish (World Precision Instruments) on the day prior to the experiment. Cells were imaged with a Leica DmI8 inverted microscope equipped with an SP8 confocal unit using a 20x dry objective (NA=0.75). Imaging was performed in an on-stage incubator chamber at 37°C, with 5% CO_2. Two independent modules were used in a sequential manner: one for bleaching, one for imaging the signal recovery. During the application of the bleaching module, the 488 laser was focused at an intensity of 5% and with a gain of 0.1% on to an area within the nucleus of each cell at maximum zoom for 20 seconds. Immediately afterwards, the first sequence was manually cancelled, the resolution was optimized, imaging area was restored to the whole cell for the second sequence. The laser power was set for optimal imaging level and images of the whole cell were acquired for 3 min circa at the rate of one image every 2.2 seconds.

Intracellular staining for flow cytometry

Cell surface staining was performed in PBS, 1% BSA (Euromedex), 1mM EDTA (GIBCO), 0.01% NaN3 (AMRESCO) (FACS Buffer) at 4°C. Viability staining (Live-Dead) with Fixable Viability Dye eFluor 780 was performed in PBS at 4°C. Cells were resuspended in FACS Buffer prior to final acquisition. Intracellular staining of γH2AX was performed using the FOXP3/Transcription Factor Staining Buffer Set (eBioscience) as per manufacturer's protocol. Cells were resuspended in FACS Buffer prior to final acquisition. All flow cytometry acquisitions were performed on the FACSVerse (BD) using the FACSSuite software (BD) and analyzed on FlowJo v10. The antibodies used are listed in **Table 4**.

802

803 Electron Microscopy

804 Cells were seeded at 5 x 10^4 cells/well in a 24w plate onto sterile 12 mm glass coverslips
805 (Thermo Scientific) and left to adhere overnight. The following morning, cells were washed in
806 PBS and were fixed using 2% glutaraldehyde in 0.1 M cacodylate buffer, pH 7.4 for 1h, post
807 fixed for 1h with 2% buffered osmium tetroxide, dehydrated in a graded series of ethanol
808 solution, and then embedded in epoxy resin. Images were acquired with a digital 4k CCD
809 camera Quemesa (EMSIS GmbH, Münster, Germany) mounted on a Tecnai Spirit transmission
810 electron microscope (ThermoFisher, Eindhoven, The Netherlands) operated at 80kV.

811

812 Micropipette aspiration microscopy

813 Prior to harvest, HeLa cell lines were incubated with 1µM SiR-DNA dye from Tebu Bio for
814 1h30 at 37°C in cell culture medium. Cells were washed, harvested and resuspended at a
815 concentration of 5x10^6 cells/mL in sterile 3% BSA in PBS-0.2% FBS. Cells were subjected to
816 the experimental conditions as described previously (Davidson et al., 2019).

817

818 Microarray Gene Expression (Affymetrix)

819 Total RNA was extracted from 10^6 HeLa cells using NucleoSpin RNA and adjusted to 50
820 ng/µL. A WT PLUS amplification and labeling protocol was conducted with 100 ng of total
821 RNA. Samples passed the quality control with a high score. The Affymetrix analysis was
822 performed by the NGS platform at Institut Curie using the Human Gene 2.0 ST chip. Human
823 Gene 2.0ST array were scanned using a Genechip 7G scanner, according to the supplier's
824 protocol. Micro-array analyses were processed with R using packages from Bioconductor. The
825 quality control was performed using ArrayQualityMetrics package without detecting any
826 outlier among the experiment. Data was normalized using the Robust Multi-Array Average

827 algorithm from the Oligo package. Annotation of the probes was done using the hugene20
828 annotation data (chip hugene20sttranscriptcluster) from Bioconductor. Differential gene-
829 expression analysis was performed with Limma. The accession number for the raw data files is
830 NCBI GEO: GSE162019.
831
832 Statistical Analysis
833 Statistical analyses were performed in Prism 7 or 8 (GraphPad Software) as indicated in the
834 figure legends.
835

836

837 **Supplementary Tables**

838

839 Table 1: Plasmids used in this study

Plasmid Name	Purpose	Insert/ Target/ Components	Reporter / Selection	Source or Identifier
pTRIP-SFFV-tagBFP-2A	Overexpression	/	BFP	(Cerboni et al., 2017)
pTRIP-SFFV-TagRFP657-2A	Overexpression	/	RFP657	This study
pTRIP-SFFV-EGFP	Overexpression	/	GFP	(Lahaye et al., 2016)
pTRIP-CMV-EGFP-2A	Overexpression	/	GFP	
pTRIP-SFFV-tagBFP-2A-SUN1	Overexpression	SUN1	BFP	This study (MGC cDNA cloneID: 40148817)
pTRIP-SFFV-tagBFP-2A-NtSUN2	Overexpression	SUN2	BFP	This study
pTRIP-SFFV-tagBFP-2A-SUN1 Dharmacon (1-298)-ntSUN2 (220-717)	Overexpression	SUN1-SUN2	BFP	This study

pTRIP-SFFV-tagBFP-2A-NtSUN2 (1-219)-SUN1 Dharmacon (299-785)	Overexpression	SUN2-SUN1	BFP	This study
pTRIP-SFFV-TagRFP657-2A-SUN1 Dharmacon	Overexpression	SUN1	RFP657	This study (MGC cDNA cloneID: 40148817
pTRIP-SFFV-TagRFP657-2A-ntSUN2	Overexpression	SUN2	RFP657	This Study
pTRIP-SFFV-EGFP-SR-KASH	Overexpression	SR-KASH	GFP	This study
pLKO1puro-shLACZ shRNA sequence: GCGATCGTAATCACCCGAGTG	Knock-down	LacZ	Puromycin	pLKO.1 clone ID TRCN0000072229
pLKO.1-Puro-LMNA sh2 shRNA sequence: GAAGCAACTTCAGGATGAGAT	Knock-down	Lamin A/C	Puromycin	pLKO.1 clone ID TRCN0000061835
pLKO.1-Puro-LMNB2 sh5 shRNA sequence:	Knock-down	Lamin B2	Puromycin	pLKO.1 clone ID TRCN0000072422

CTACAAGTTCACGCC CAAGTA				
pCMV-VSVG	Expression	VSV-G	/	(Manel et al., 2010)
psPAX2	Packaging vector	/	/	(Manel et al., 2010)
HIVGFP (NL4-3 strain)	Infection	Vif-, Vpr-, Vpu-, Env-, Nef-	GFP in Nef	(Manel et al., 2010)
HIVGFP N74D	Infection	Vif-, Vpr-, Vpu-, Env-, Nef-, CA mutation N74D	GFP in Nef	(Lahaye et al., 2016)
HIVGFP env-nef-	Infection	Vif+, Vpr+, Vpu+, Env-, Nef-	GFP in Nef	This study
HIVGFP env- nef- vpr-	Infection	Vif+, Vpr-, Vpu+, Env-, Nef-	GFP in Nef	This study
HIV-mTagBFP2 (NL4-3 strain)	Infection	Vif-, Vpr-, Vpu-, Env-, Nef-	BFP in Nef	This study

HIV-2 ROD9 ΔenvΔnef mTagBFP2+	Infection	Vif+, Vpr+, Vpx+, Env-, Nef-	BFP in Nef	This study
HIV-2 ROD9 ΔenvΔnef GFP	Infection	Vif+, Vpr+, Vpx+, Env-, Nef-	GFP in Nef	(Manel et al., 2010)
pSIV3+	Helper plasmid		/	(Mangeot et al., 2000)

840

841 Table 2: Drugs used in cell culture in this study

Name	**Description**	**Cat. Reference**	**Company**	**Final Concentration**
Cyclosporin A	Inhibits CypA-CA interaction	S2286	Selleckchem	2 µM
AZT	Reverse transcriptase inhibitor	A2169	Sigma	24 µM
NVP	Reverse transcriptase inhibitor	SML0097	Sigma	10 µM
Etoposide	Topoisomerase II inhibitor	E1383	Sigma	5, 50 or 500 µM
Q-VD-Oph	Pan-caspase inhibitor	S7311	Selleckchem	50 µM
AZD6738	ATR inhibitor	S7693	Selleckchem	1 µM

DMSO	Diluent	BDH1115	VWR Chemicals	adjusted

842

843

844 Table 3: Primers used for HIV DNA species Real Time Quantitiative PCR

Strain	**Amplification**	**Primer name**	**Sequence**	**Annealing**
Human	Beta-globin	bglobin-f	CCCTTGGACCCAGAGGTTCT	50°C
Human	Beta-globin	bglobin-r	CGAGCACTTTCTTGCCATGA	50°C
HIV-1	Total DNA (Late RT)	hiv1-3'U3-fwd	GCATGGAATGGATGACCCTGAGA	65°C
HIV-1	Total DNA (Late RT)	hiv1-psi-rev2	CGTCGAGAGATCTCCTCT GGCTTTA	65°C
HIV-1	2-LTR circles	Junct4 - fwd	CAGTGTGGAAAATCTCTA GCAGTACTG	65°C
HIV-1	2-LTR circles	hiv1-psi-rev2	CGTCGAGAGATCTCCTCT GGCTTTA	65°C
HIV-1	Integrated DNA round 1	alu1	GCCTCCCAAAGTGCT GGGATTACAG	65°C
HIV-1	Integrated DNA round 1	hiv1-psi-rev2	CGTCGAGAGATCTCCTCT GGCTTTA	65°C

HIV-1	Integrated DNA round 2	hiv1-f2	CTGGGAGCTCTCTGGCTAACTA	65°C
HIV-1	Integrated DNA round 2	hiv1-r2	AACAGACGGGCACACACTACTT	65°C
HIV-2	Total DNA (Late RT)	hiv2-3'U3-fwd	GAAGGGATGTTTT ACCATTTAGTTA	65°C
HIV-2	Total DNA (Late RT)	hiv2-psi-rev	GTTCCAAGACTTCTCAGTCTTCTT C	65°C
HIV-2	2-LTR circles	hiv2-R-fwd	GTTCTCTCCAGCACTAGCAGGTA	65°C
HIV-2	2-LTR circles	hiv2-3'U3-rev	TAACTAAATGGTA AAACATCCCTTC	65°C
HIV-2	Integrated DNA round 1	alu1	GCCTCCCAAAGTGCT GGGATTACAG	65°C
HIV-2	Integrated DNA round 1	hiv2-r1	AAGGGTCCTAACAGACCAGGGTC T	65°C
HIV-2	Integrated DNA round 2	hiv2-f2	GCAGGTAGAGCCTGGGTGTTC	65°C
HIV-2	Integrated DNA round 2	hiv2-r2	CAGGCGGCGACTAGGAGAGAT	65°C

845

846

847 Table 4: Antibodies used in this study for Western Blot, Confocal Imaging and Flow

848 Cytometry

Antibody target	Cat. Reference	Company	Application
Actin	MAB1501 Clone C4	Sigma	WB (1:5000)
Vinculin	V9264	Sigma	WB (1:5000)
SUN1	ab124770	Abcam	WB (1:1000)
SUN2	HPA001209	Atlas antibodies	WB (1:1000)
SUN2	ABT272	Millipore	WB (1:1000)
Lamin A/C	SAB4200236	Sigma	WB (1:1000)
Lamin B2	ab8983 clone LN43	Abcam	WB (1:1000)
NUP153	HPA027896	Sigma	IF (1:50)
SiR-DNA staining	SC007	Tebu Bio	Live imaging (1µM)
H2AX p-S139	562377 Clone N1-431	BD	Coupled to PE; FACS (1:100)
Mouse IgG1 κ isotype control	554680 Clone MOPC-21	BD	Coupled to PE; FACS (1:100)
Rabbit-IgG (H+L)	A-11010	Invitrogen	Alexa Fluor 546 for IF (1:200)
Rabbit-IgG	7074S	Ozyme	Conjugated to HRP for WB (1:10000)
Mouse IgG	7076S	Ozyme	Conjugated to HRP for WB (1:10000)

849

References

Ariumi, Y., Turelli, P., Masutani, M., and Trono, D. (2005). DNA Damage Sensors ATM, ATR, DNA-PKcs, and PARP-1 Are Dispensable for Human Immunodeficiency Virus Type 1 Integration. J. Virol. *79*, 2973–2978.

Bhargava, A., Lahaye, X., and Manel, N. (2018). Let me in: Control of HIV nuclear entry at the nuclear envelope. Cytokine Growth Factor Rev. *40*, 59–67.

Braaten, D., and Luban, J. (2001). Cyclophilin A regulates HIV-1 infectivity, as demonstrated by gene targeting in human T cells. EMBO J *20*, 1300–1309.

Burke, B., and Stewart, C.L. (2013). The nuclear lamins: flexibility in function. Nat. Rev. Mol. Cell Biol. *14*, 13–24.

Cerboni, S., Jeremiah, N., Gentili, M., Gehrmann, U., Conrad, C., Stolzenberg, M.C., Picard, C., Neven, B., Fischer, A., Amigorena, S., et al. (2017). Intrinsic antiproliferative activity of the innate sensor STING in T lymphocytes. J Exp Med.

Davidson, P.M., Fedorchak, G.R., Mondésert-Deveraux, S., Bell, E.S., Isermann, P., Aubry, D., Allena, R., and Lammerding, J. (2019). High-throughput microfluidic micropipette aspiration device to probe time-scale dependent nuclear mechanics in intact cells. Lab. Chip *19*, 3652–3663.

De Iaco, A., and Luban, J. (2014). Cyclophilin A promotes HIV-1 reverse transcription but its effect on transduction correlates best with its effect on nuclear entry of viral cDNA. Retrovirology *11*, 11.

DeHart, J.L., Andersen, J.L., Zimmerman, E.S., Ardon, O., An, D.S., Blackett, J., Kim, B., and Planelles, V. (2005). The Ataxia Telangiectasia-Mutated and Rad3-Related Protein Is Dispensable for Retroviral Integration. J. Virol. *79*, 1389–1396.

Dharan, A., Bachmann, N., Talley, S., Zwikelmaier, V., and Campbell, E.M. (2020). Nuclear pore blockade reveals that HIV-1 completes reverse transcription and uncoating in the nucleus. Nat. Microbiol. *5*, 1088–1095.

Donahue, D.A., Amraoui, S., di Nunzio, F., Kieffer, C., Porrot, F., Opp, S., Diaz-Griffero, F., Casartelli, N., and Schwartz, O. (2016). SUN2 Overexpression Deforms Nuclear Shape and Inhibits HIV. J. Virol. *90*, 4199–4214.

Donahue, D.A., Porrot, F., Couespel, N., and Schwartz, O. (2017). SUN2 Silencing Impairs CD4 T Cell Proliferation and Alters Sensitivity to HIV-1 Infection Independently of Cyclophilin A. J. Virol. *91*.

Ebina, H., Kanemura, Y., Suzuki, Y., Urata, K., Misawa, N., and Koyanagi, Y. (2012). Integrase-independent HIV-1 infection is augmented under conditions of DNA damage and produces a viral reservoir. Virology *427*, 44–50.

Foote, K.M., Nissink, J.W.M., McGuire, T., Turner, P., Guichard, S., Yates, J.W.T., Lau, A., Blades, K., Heathcote, D., Odedra, R., et al. (2018). Discovery and Characterization of AZD6738, a Potent Inhibitor of Ataxia Telangiectasia Mutated and Rad3 Related (ATR) Kinase with Application as an Anticancer Agent. J. Med. Chem. *61*, 9889–9907.

Goh, W.C., Rogel, M.E., Kinsey, C.M., Michael, S.F., Fultz, P.N., Nowak, M.A., Hahn, B.H., and Emerman, M. (1998). HIV-1 Vpr increases viral expression by manipulation of the cell cycle: a mechanism for selection of Vpr in vivo. Nat. Med. *4*, 65–71.

Gonzalo, S. (2014). DNA Damage and Lamins. In Cancer Biology and the Nuclear Envelope,

E.C. Schirmer, and J.I. de las Heras, eds. (New York, NY: Springer New York), pp. 377–399.

Ji, J.Y., Lee, R.T., Vergnes, L., Fong, L.G., Stewart, C.L., Reue, K., Young, S.G., Zhang, Q., Shanahan, C.M., and Lammerding, J. (2007). Cell Nuclei Spin in the Absence of Lamin B1. J. Biol. Chem. *282*, 20015–20026.

Kidiyoor, G.R., Li, Q., Bastianello, G., Bruhn, C., Giovannetti, I., Mohamood, A., Beznoussenko, G.V., Mironov, A., Raab, M., Piel, M., et al. (2020). ATR is essential for preservation of cell mechanics and nuclear integrity during interstitial migration. Nat. Commun. *11*, 4828.

Koyama, T., Sun, B., Tokunaga, K., Tatsumi, M., and Ishizaka, Y. (2013). DNA damage enhances integration of HIV-1 into macrophages by overcoming integrase inhibition. Retrovirology *10*, 21.

Kumar, A., Mazzanti, M., Mistrik, M., Kosar, M., Beznoussenko, G.V., Mironov, A.A., Garrè, M., Parazzoli, D., Shivashankar, G.V., Scita, G., et al. (2014). ATR mediates a checkpoint at the nuclear envelope in response to mechanical stress. Cell *158*, 633–646.

Lahaye, X., Satoh, T., Gentili, M., Cerboni, S., Conrad, C., Hurbain, I., El Marjou, A., Lacabaratz, C., Lelievre, J.D., and Manel, N. (2013). The capsids of HIV-1 and HIV-2 determine immune detection of the viral cDNA by the innate sensor cGAS in dendritic cells. Immunity *39*, 1132–1142.

Lahaye, X., Satoh, T., Gentili, M., Cerboni, S., Silvin, A., Conrad, C., Ahmed-Belkacem, A., Rodriguez, E.C., Guichou, J.-F., Bosquet, N., et al. (2016). Nuclear Envelope Protein SUN2 Promotes Cyclophilin-A-Dependent Steps of HIV Replication. Cell Rep. *15*, 879–892.

Lammerding, J., Schulze, P.C., Takahashi, T., Kozlov, S., Sullivan, T., Kamm, R.D., Stewart, C.L., and Lee, R.T. (2004). Lamin A/C deficiency causes defective nuclear mechanics and mechanotransduction. J. Clin. Invest. *113*, 370–378.

Lawrence, K.S., Tapley, E.C., Cruz, V.E., Li, Q., Aung, K., Hart, K.C., Schwartz, T.U., Starr, D.A., and Engebrecht, J. (2016). LINC complexes promote homologous recombination in part through inhibition of nonhomologous end joining. J. Cell Biol. *215*, 801–821.

Lei, K., Zhang, X., Ding, X., Guo, X., Chen, M., Zhu, B., Xu, T., Zhuang, Y., Xu, R., and Han, M. (2009). SUN1 and SUN2 play critical but partially redundant roles in anchoring nuclei in skeletal muscle cells in mice. Proc Natl Acad Sci U A *106*, 10207–10212.

Lei, K., Zhu, X., Xu, R., Shao, C., Xu, T., Zhuang, Y., and Han, M. (2012). Inner nuclear envelope proteins SUN1 and SUN2 play a prominent role in the DNA damage response. Curr Biol *22*, 1609–1615.

Liu, Q., Pante, N., Misteli, T., Elsagga, M., Crisp, M., Hodzic, D., Burke, B., and Roux, K.J. (2007). Functional association of Sun1 with nuclear pore complexes. J Cell Biol *178*, 785–798.

Lottersberger, F., Karssemeijer, R.A., Dimitrova, N., and de Lange, T. (2015). 53BP1 and the LINC Complex Promote Microtubule-Dependent DSB Mobility and DNA Repair. Cell *163*, 880–893.

Luo, X., Yang, W., and Gao, G. (2018). SUN1 Regulates HIV-1 Nuclear Import in a Manner Dependent on the Interaction between the Viral Capsid and Cellular Cyclophilin A. J. Virol. *92*, e00229-18.

Manel, N., Hogstad, B., Wang, Y., Levy, D.E., Unutmaz, D., and Littman, D.R. (2010). A cryptic sensor for HIV-1 activates antiviral innate immunity in dendritic cells. Nature *467*,

214–217.

Mangeot, P.E., Negre, D., Dubois, B., Winter, A.J., Leissner, P., Mehtali, M., Kaiserlian, D., Cosset, F.L., and Darlix, J.L. (2000). Development of minimal lentivirus vectors derived from simian immunodeficiency virus (SIVmac251) and their use for gene transfer into human dendritic cells. J Virol *74*, 8307–8315.

Mlcochova, P., Caswell, S.J., Taylor, I.A., Towers, G.J., and Gupta, R.K. (2018). DNA damage induced by topoisomerase inhibitors activates SAMHD1 and blocks HIV-1 infection of macrophages. EMBO J. *37*, 50–62.

de Noronha, C.M., Sherman, M.P., Lin, H.W., Cavrois, M.V., Moir, R.D., Goldman, R.D., and Greene, W.C. (2001). Dynamic disruptions in nuclear envelope architecture and integrity induced by HIV-1 Vpr. Science *294*, 1105–1108.

Oza, P., Jaspersen, S.L., Miele, A., Dekker, J., and Peterson, C.L. (2009). Mechanisms that regulate localization of a DNA double-strand break to the nuclear periphery. Genes Dev. *23*, 912–927.

Procter, D.J., Banerjee, A., Nukui, M., Kruse, K., Gaponenko, V., Murphy, E.A., Komarova, Y., and Walsh, D. (2018). The HCMV Assembly Compartment Is a Dynamic Golgi-Derived MTOC that Controls Nuclear Rotation and Virus Spread. Dev. Cell *45*, 83-100.e7.

Ranade, D., Pradhan, R., Jayakrishnan, M., Hegde, S., and Sengupta, K. (2019). Lamin A/C and Emerin depletion impacts chromatin organization and dynamics in the interphase nucleus. BMC Mol. Cell Biol. *20*, 11.

Rello-Varona, S., Gámez, A., Moreno, V., Stockert, J.C., Cristóbal, J., Pacheco, M., Cañete, M., Juarranz, Á., and Villanueva, Á. (2006). Metaphase arrest and cell death induced by etoposide on HeLa cells. Int. J. Biochem. Cell Biol. *38*, 2183–2195.

Roshal, M., Kim, B., Zhu, Y., Nghiem, P., and Planelles, V. (2003). Activation of the ATR-mediated DNA Damage Response by the HIV-1 Viral Protein R. J. Biol. Chem. *278*, 25879–25886.

Schaller, T., Ocwieja, K.E., Rasaiyaah, J., Price, A.J., Brady, T.L., Roth, S.L., Hué, S., Fletcher, A.J., Lee, K., KewalRamani, V.N., et al. (2011). HIV-1 Capsid-Cyclophilin Interactions Determine Nuclear Import Pathway, Integration Targeting and Replication Efficiency. PLoS Pathog. *7*, e1002439.

Schaller, T., Bulli, L., Pollpeter, D., Betancor, G., Kutzner, J., Apolonia, L., Herold, N., Burk, R., and Malim, M.H. (2017). Effects of Inner Nuclear Membrane Proteins SUN1/UNC-84A and SUN2/UNC-84B on the Early Steps of HIV-1 Infection. J. Virol. *91*, e00463-17, e00463-17.

Schindelin, J., Arganda-Carreras, I., Frise, E., Kaynig, V., Longair, M., Pietzsch, T., Preibisch, S., Rueden, C., Saalfeld, S., Schmid, B., et al. (2012). Fiji: an open-source platform for biological-image analysis. Nat Methods *9*, 676–682.

Schoggins, J.W., Wilson, S.J., Panis, M., Murphy, M.Y., Jones, C.T., Bieniasz, P., and Rice, C.M. (2011). A diverse range of gene products are effectors of the type I interferon antiviral response. Nature *472*, 481–485.

Singh, M., Hunt, C.R., Pandita, R.K., Kumar, R., Yang, C.-R., Horikoshi, N., Bachoo, R., Serag, S., Story, M.D., Shay, J.W., et al. (2013). Lamin A/C depletion enhances DNA damage-induced stalled replication fork arrest. Mol. Cell. Biol. *33*, 1210–1222.

Starr, T.K., Jameson, S.C., and Hogquist, K.A. (2003). Positive and negative selection of T

cells. Annu Rev Immunol *21*, 139–176.

Sun, W.-W., Jiao, S., Sun, L., Zhou, Z., Jin, X., and Wang, J.-H. (2018). SUN2 Modulates HIV-1 Infection and Latency through Association with Lamin A/C To Maintain the Repressive Chromatin. MBio *9*, e02408-17, /mbio/9/3/mBio.02408-17.atom.

Tseng, Q., Duchemin-Pelletier, E., Deshiere, A., Balland, M., Guillou, H., Filhol, O., and Thery, M. (2012). Spatial organization of the extracellular matrix regulates cell-cell junction positioning. Proc. Natl. Acad. Sci. *109*, 1506–1511.

Yamashita, M., and Engelman, A.N. (2017). Capsid-Dependent Host Factors in HIV-1 Infection. Trends Microbiol. *25*, 741–755.

Zhu, R., Antoku, S., and Gundersen, G.G. (2017). Centrifugal Displacement of Nuclei Reveals Multiple LINC Complex Mechanisms for Homeostatic Nuclear Positioning. Curr. Biol. CB *27*, 3097-3110.e5.

Zimmerman, E.S., Sherman, M.P., Blackett, J.L., Neidleman, J.A., Kreis, C., Mundt, P., Williams, S.A., Warmerdam, M., Kahn, J., Hecht, F.M., et al. (2006). Human immunodeficiency virus type 1 Vpr induces DNA replication stress in vitro and in vivo. J. Virol. *80*, 10407–10418.

Figure 1

Figure 2

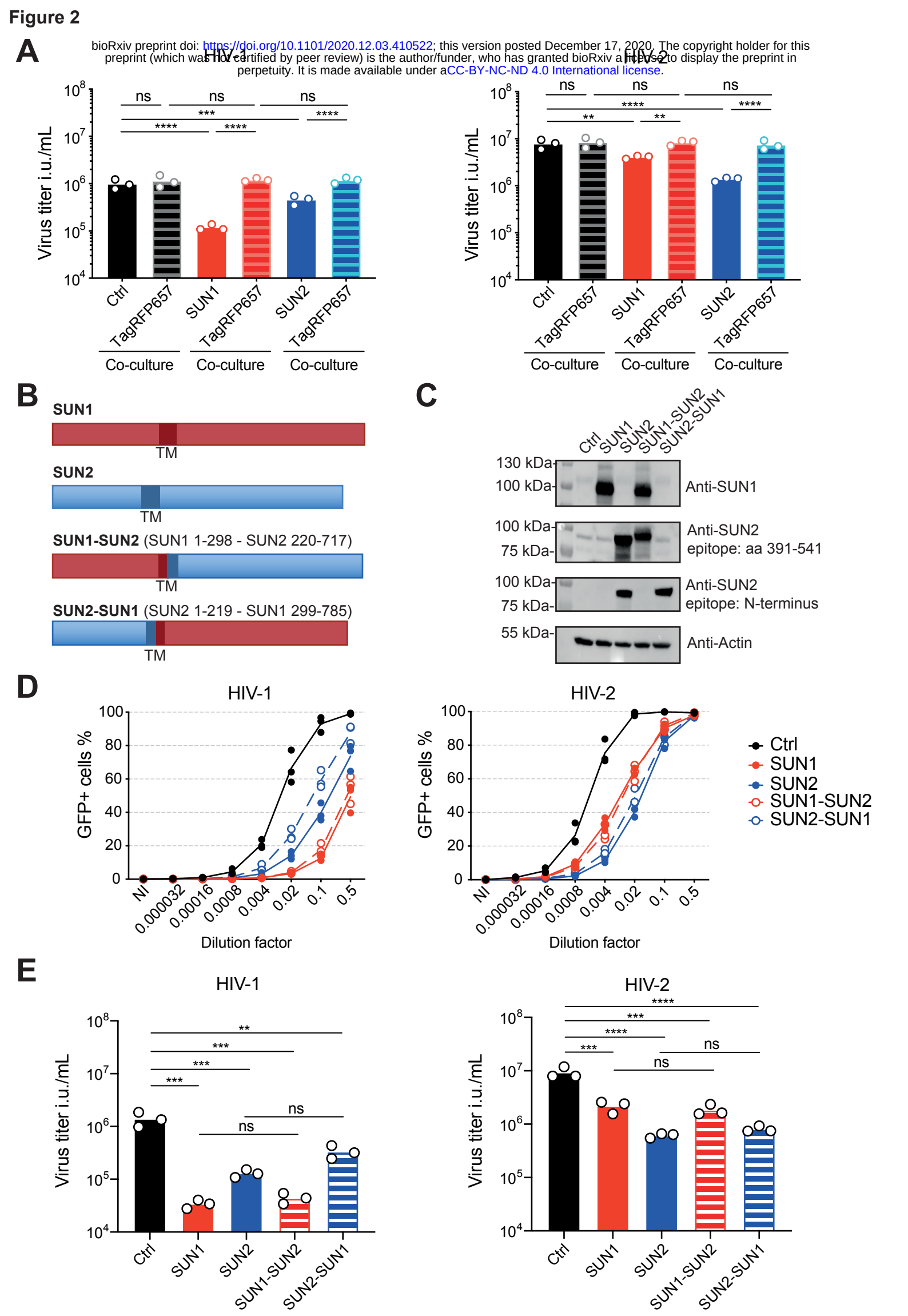

Figure 3

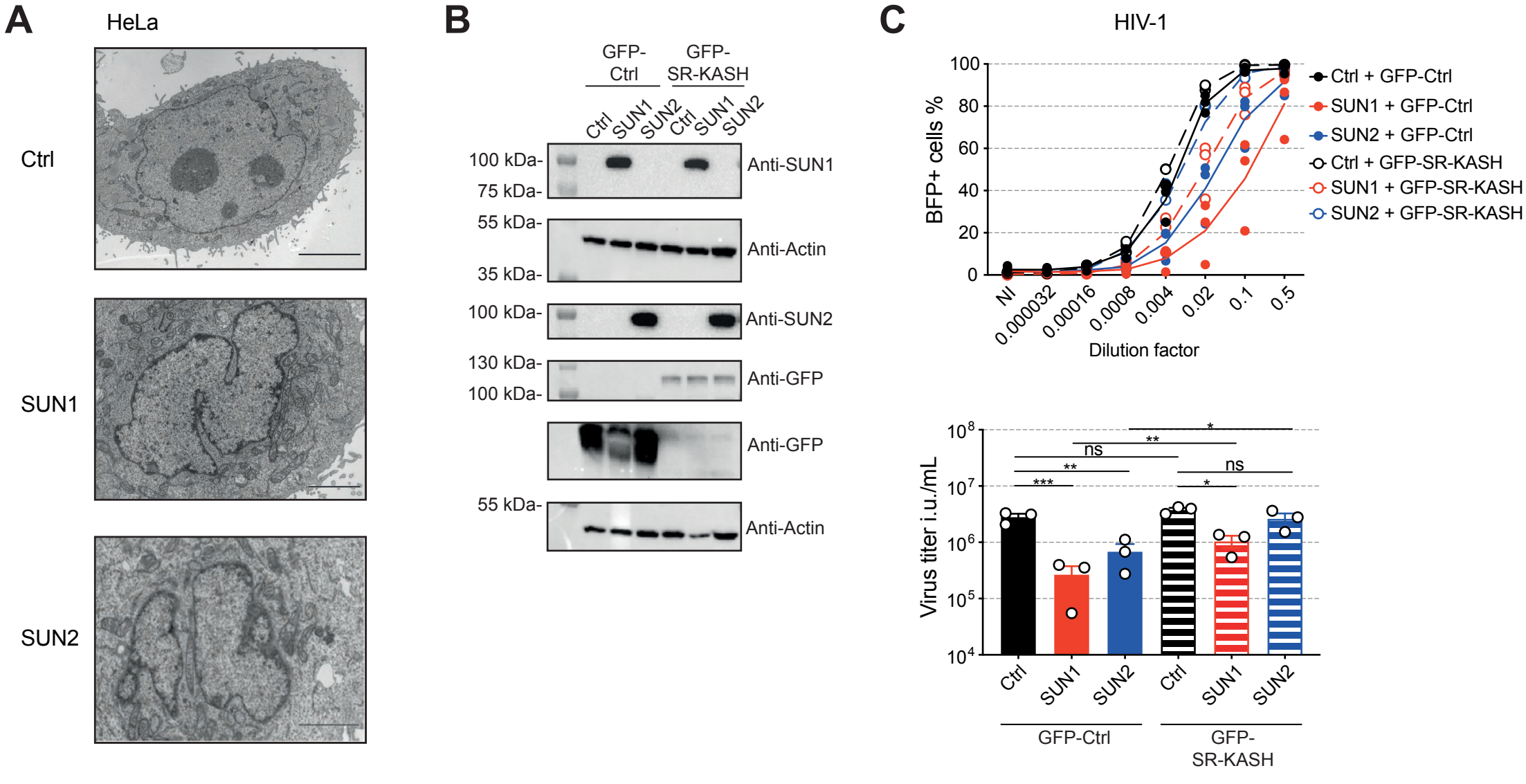
A
HeLa
Ctrl
SUN1
SUN2
B
GFP-Ctrl
GFP-SR-KASH
Ctrl
SUN1
SUN2
Ctrl
SUN1
SUN2
100 kDa-
75 kDa-
Anti-SUN1
55 kDa-
35 kDa-
Anti-Actin
100 kDa-
Anti-SUN2
130 kDa-
100 kDa-
Anti-GFP
Anti-GFP
55 kDa-
Anti-Actin
C
HIV-1
BFP+ cells %
100
80
60
40
20
0
NI
0.000032
0.00016
0.0008
0.004
0.02
0.1
0.5
Dilution factor
Ctrl + GFP-Ctrl
SUN1 + GFP-Ctrl
SUN2 + GFP-Ctrl
Ctrl + GFP-SR-KASH
SUN1 + GFP-SR-KASH
SUN2 + GFP-SR-KASH
Virus titer i.u./mL
10^8
10^7
10^6
10^5
10^4
ns
**
***
*
ns
*
Ctrl
SUN1
SUN2
Ctrl
SUN1
SUN2
GFP-Ctrl
GFP-SR-KASH

Figure 4

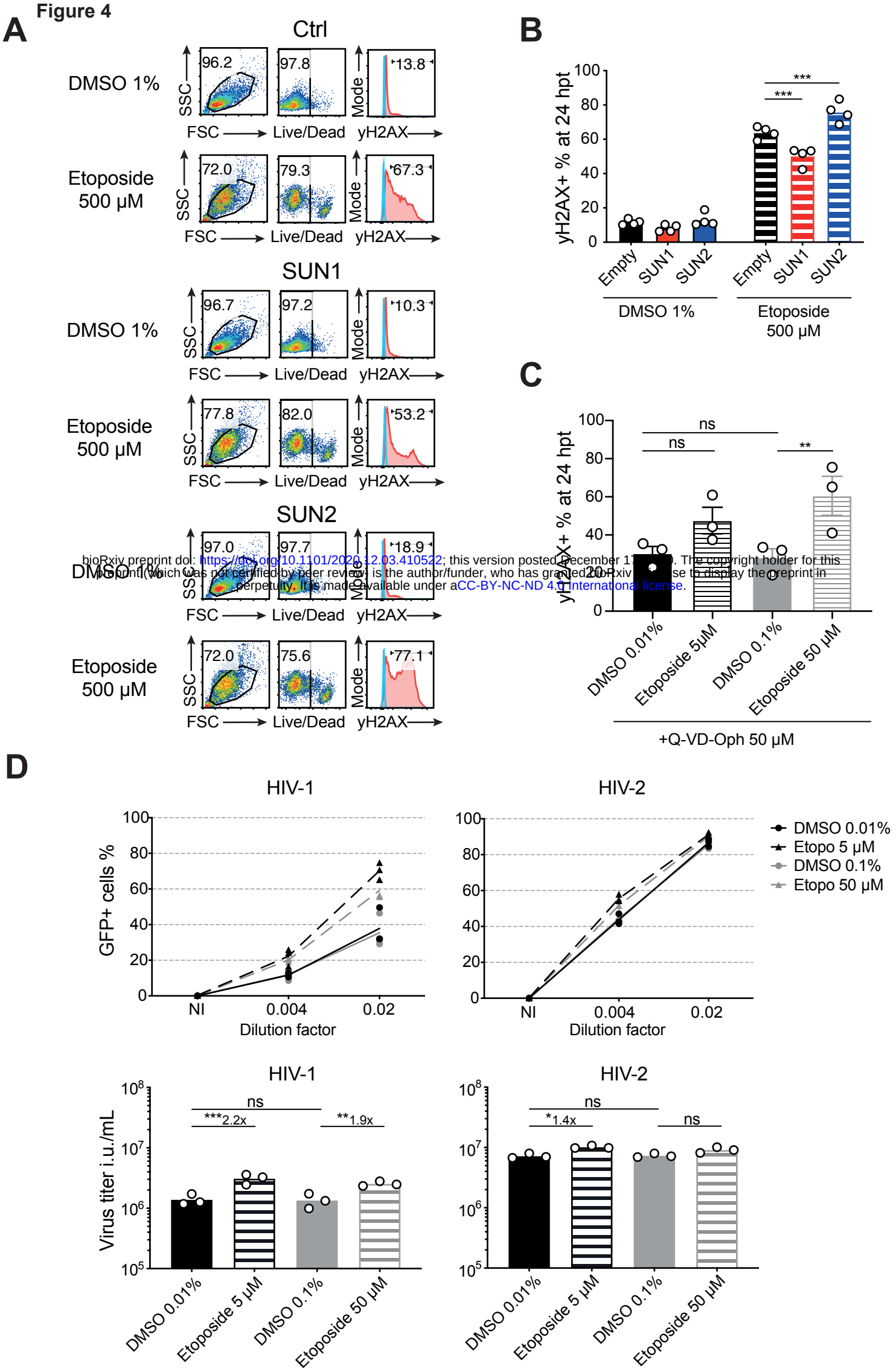

Figure 5

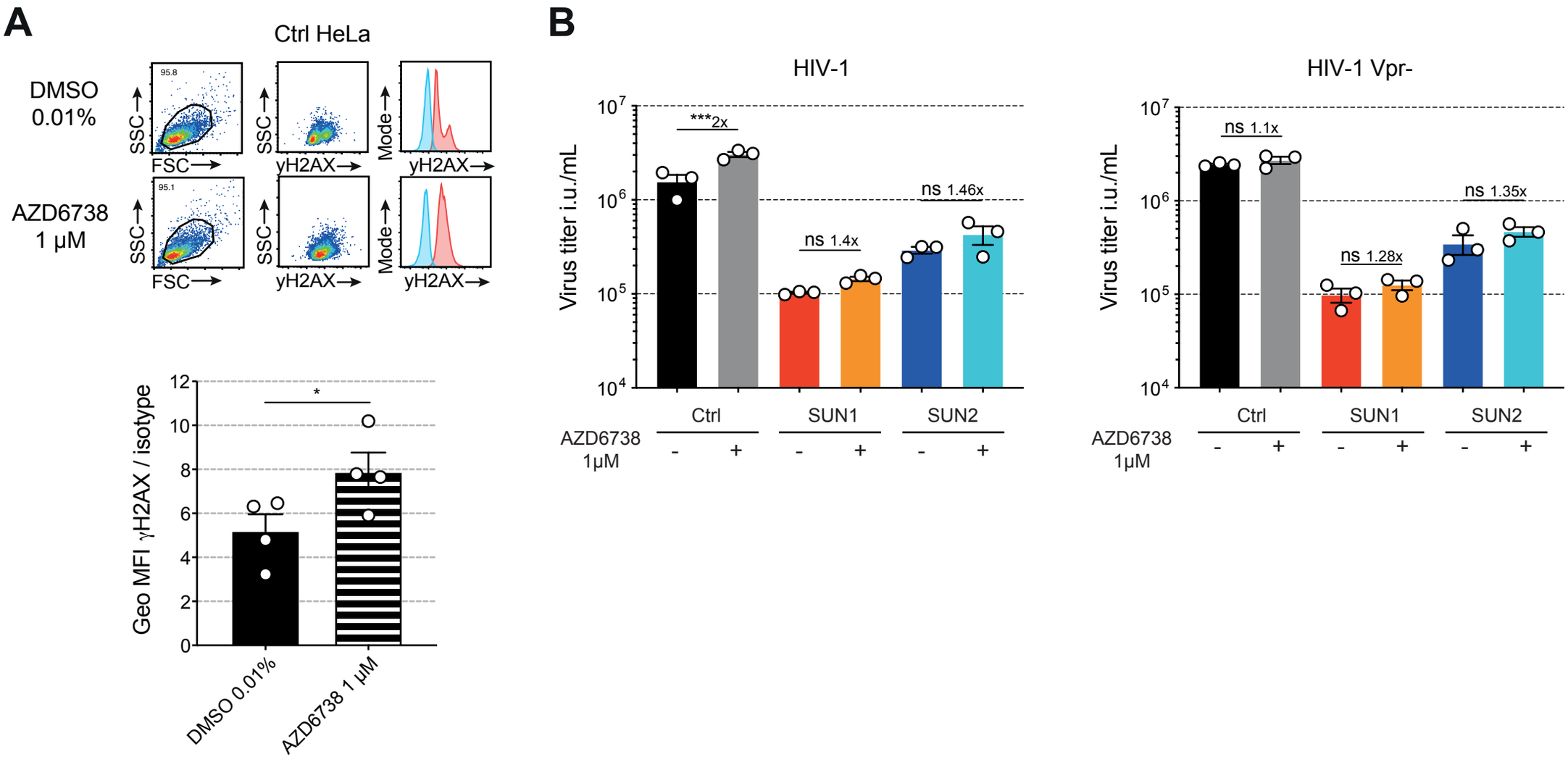
A
Ctrl HeLa
DMSO
0.01%
AZD6738
1 µM
95.8
95.1
SSC
FSC
yH2AX
Mode
Geo MFI γH2AX / isotype
*
DMSO 0.01%
AZD6738 1 µM
B
HIV-1
HIV-1 Vpr-
Virus titer i.u./mL
***2x
ns 1.4x
ns 1.46x
ns 1.1x
ns 1.28x
ns 1.35x
Ctrl
SUN1
SUN2
AZD6738
1µM

Figure 6

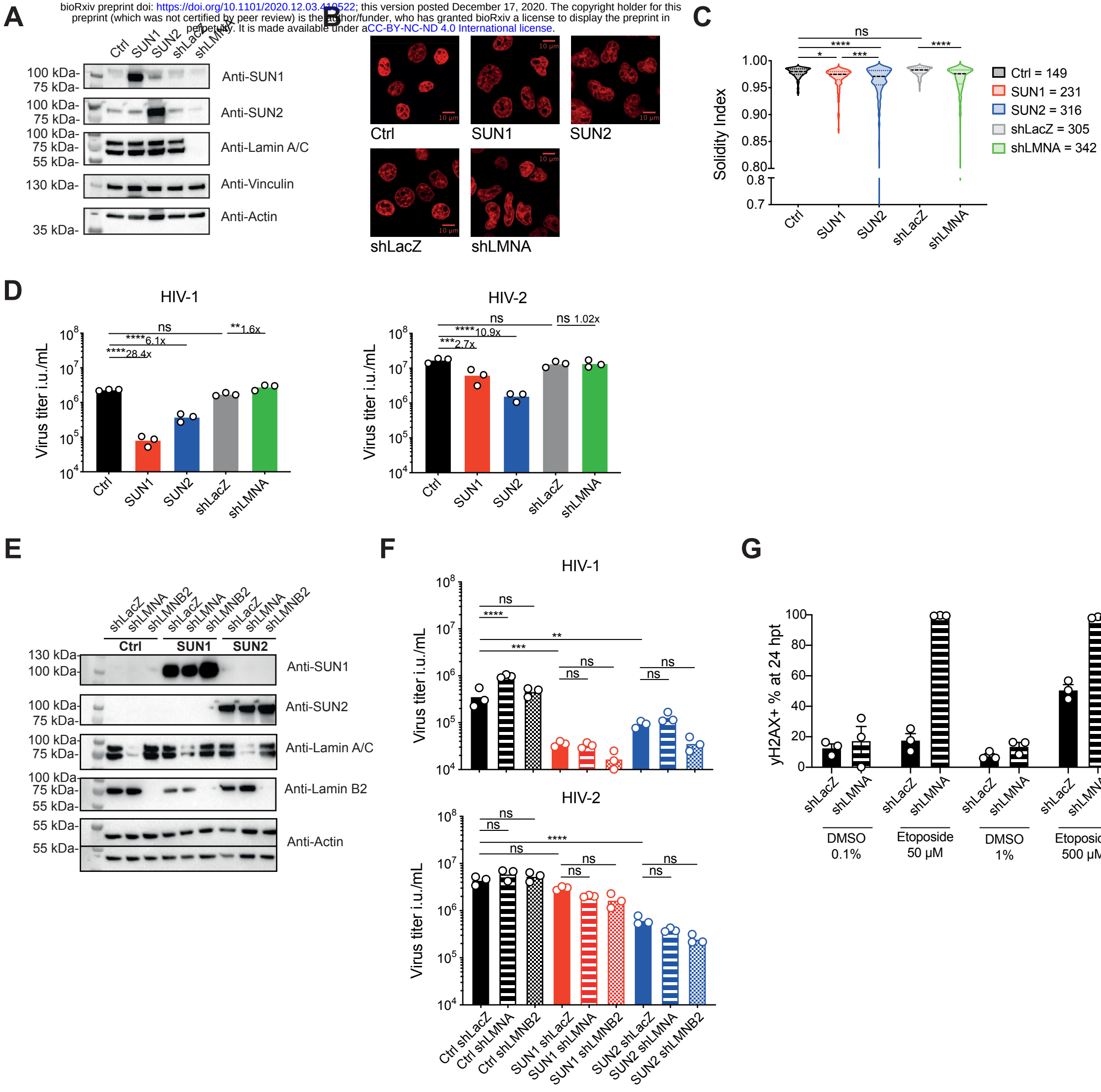

Figure 7

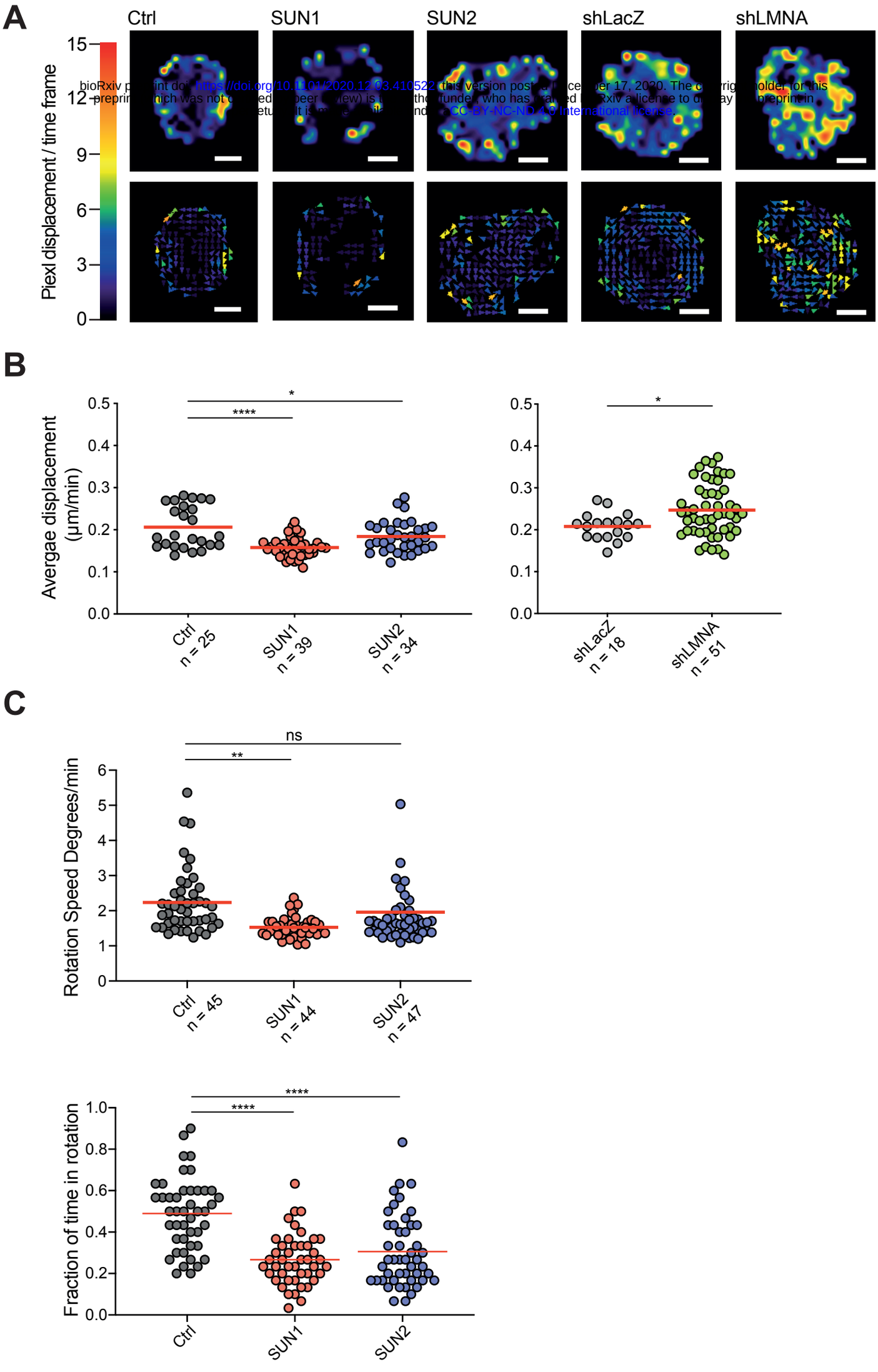

Figure S1

A

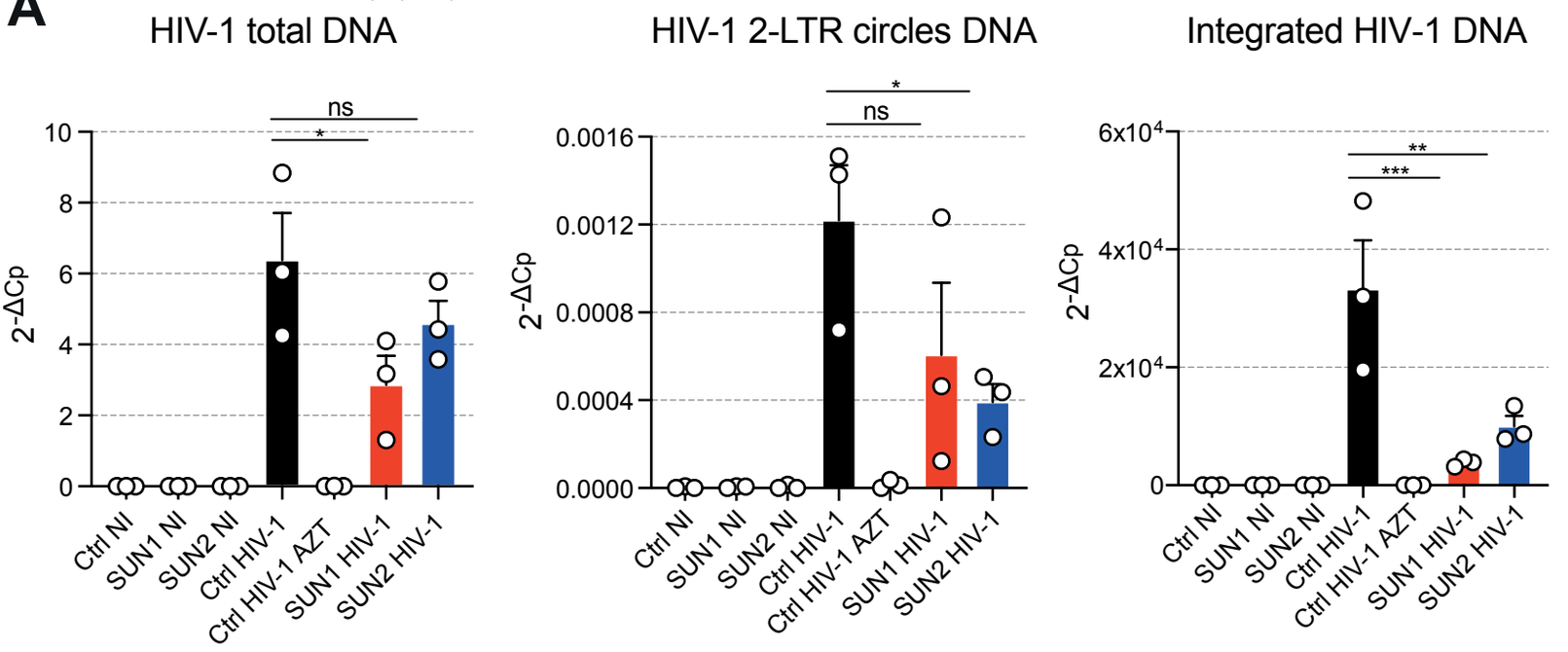

B

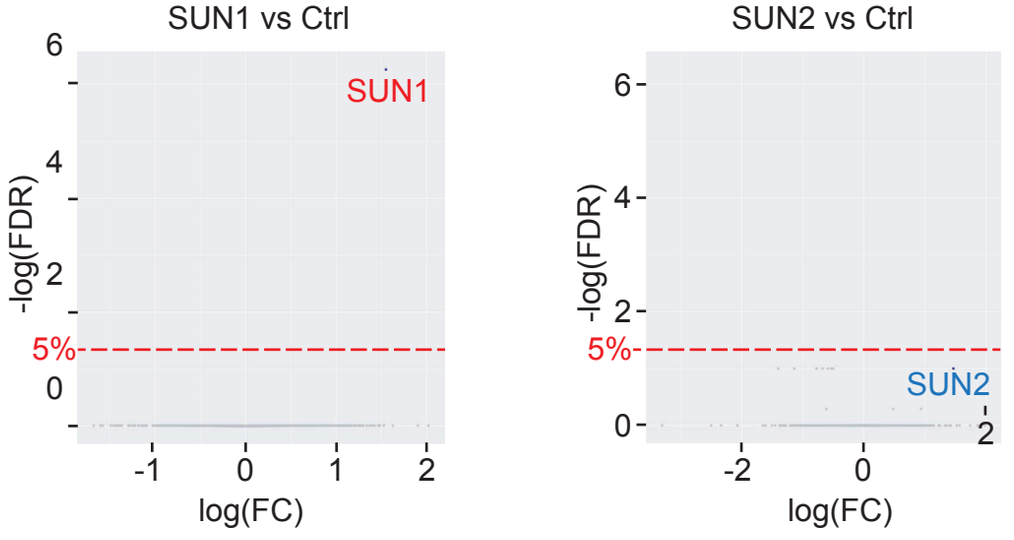

Figure S2

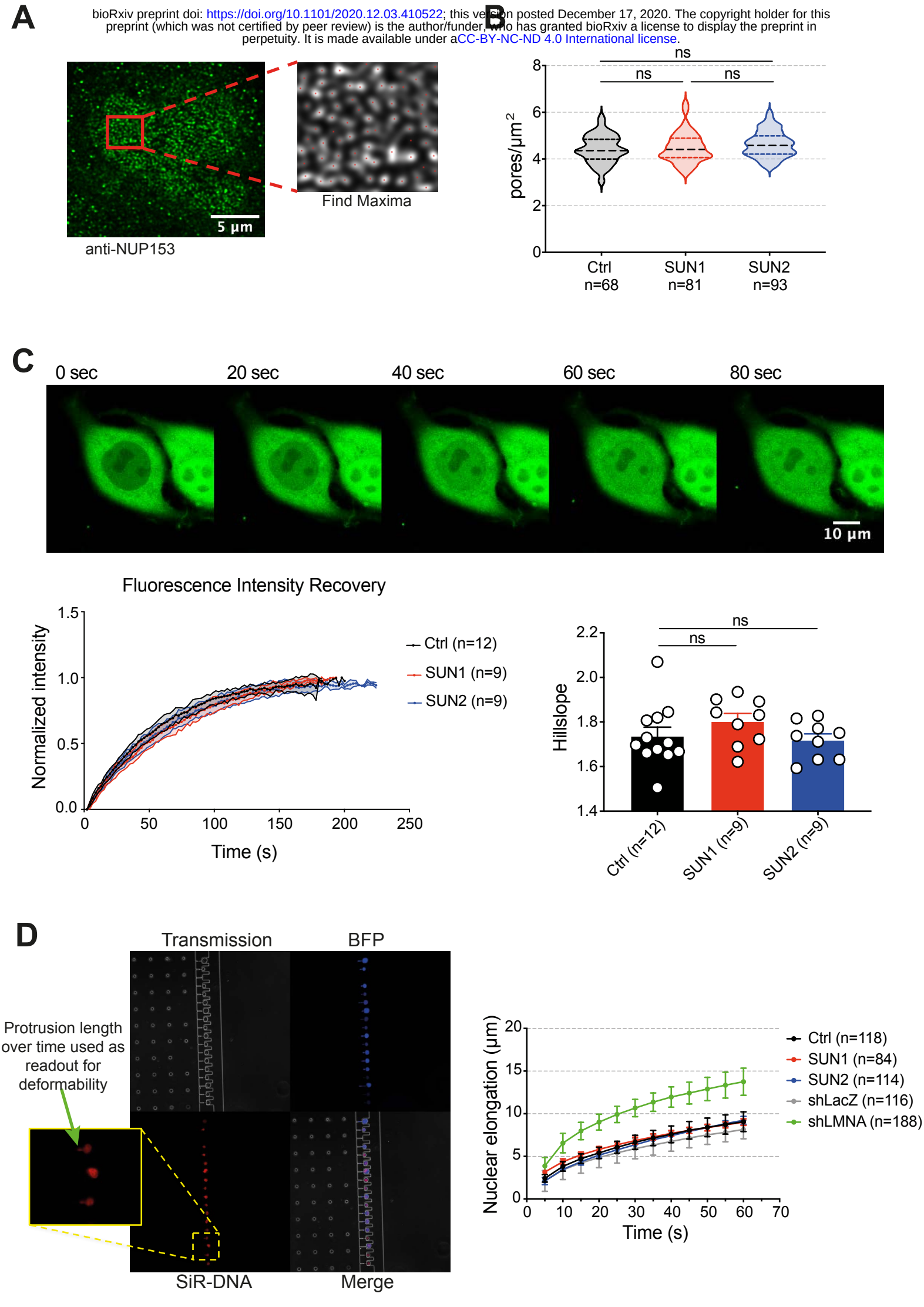

Figure S3

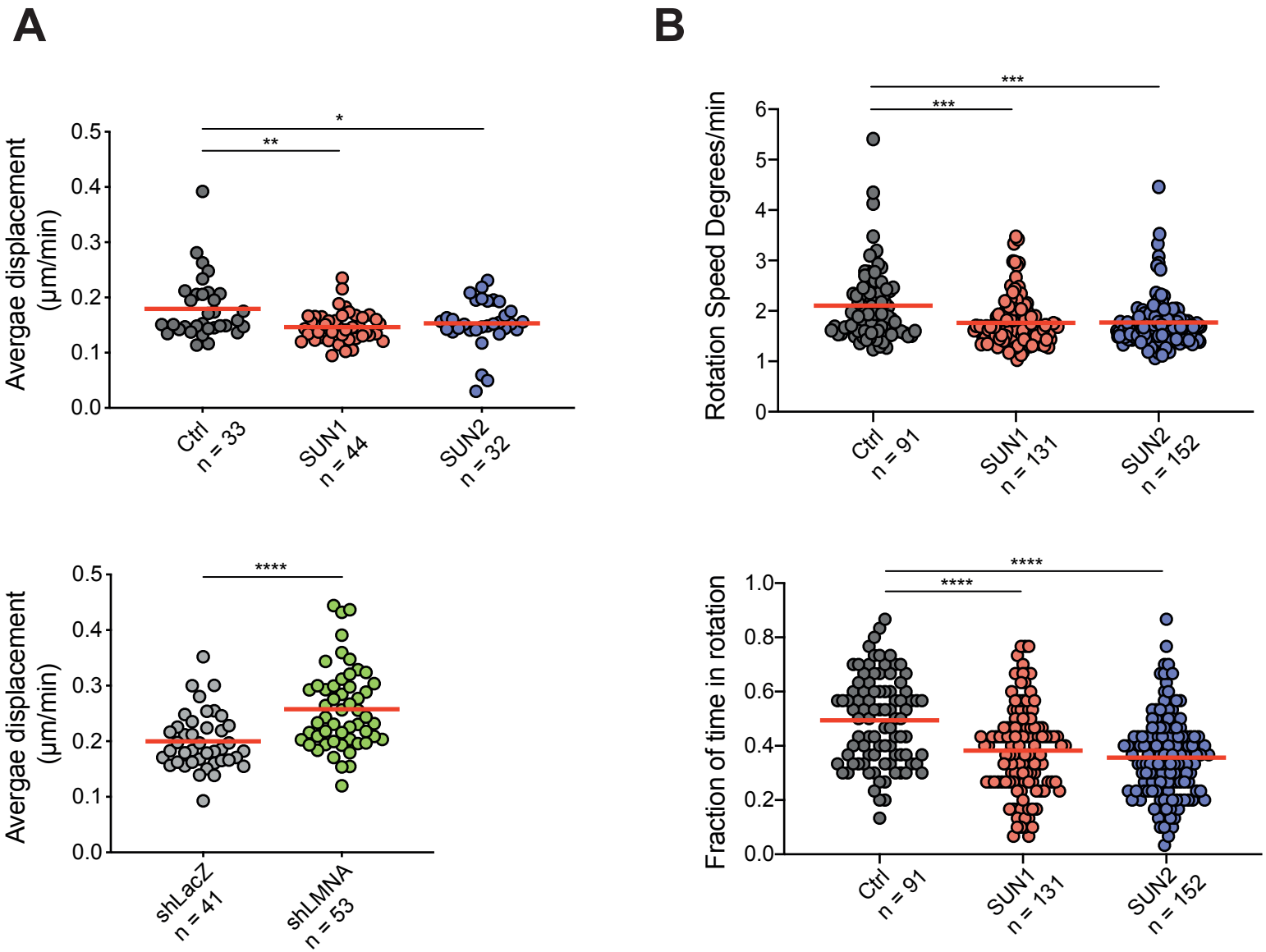
A
B
Avergae displacement (µm/min)
0.5
0.4
0.3
0.2
0.1
0.0
*
**
Ctrl n = 33
SUN1 n = 44
SUN2 n = 32
Rotation Speed Degrees/min
6
5
4
3
2
1
0
***
***
Ctrl n = 91
SUN1 n = 131
SUN2 n = 152
Avergae displacement (µm/min)
****
shLacZ n = 41
shLMNA n = 53
Fraction of time in rotation
1.0
0.8
0.6
0.4
0.2
0.0
****
****
Ctrl n = 91
SUN1 n = 131
SUN2 n = 152